MNRAS 000, 1–21 (2020) Preprint 21 October 2021 Compiled using MNRAS LATEX style file v3.0

New Optically Identified Supernova Remnants in the Large Magellanic Cloud

Miranda Yew[1], Miroslav D. Filipović[1,★] Milorad Stupar[1], Sean D. Points[2], Manami Sasaki[3], Pierre Maggi[4], Frank Haberl[5], Patrick J. Kavanagh[6], Quentin A. Parker[7,8], Evan J. Crawford[1], Branislav Vukotić[9], Dejan Urošević[10,11], Hidetoshi Sano[12,13], Ivo R. Seitenzahl[14], Gavin Rowell[15], Denis Leahy[16], Luke M. Bozzetto[1], Chandreyee Maitra[5], Howard Leverenz[1], Jeffrey L. Payne[1], Laurence A. F. Park[1], Rami Z. E. Alsaberi[1] and Thomas G. Pannuti[17]

[1]*Western Sydney University, Locked Bag 1797, Penrith South DC, NSW 2751, Australia*
[2]*Cerro Tololo Inter-American Observatory/NSF's NOIRLab, Casilla 603, La Serena, Chile*
[3]*Remeis Observatory and ECAP, Universität Erlangen-Nürnberg, Sternwartstraße 7, D-96049 Bamberg, Germany*
[4]*Observatoire Astronomique de Strasbourg, Université de Strasbourg, CNRS, 11 rue de l'Université, F-67000 Strasbourg, France*
[5]*Max-Planck-Institut für extraterrestrische Physik, Gießenbachstraße 1, D-85748 Garching, Germany*
[6]*School of Cosmic Physics, Dublin Institute for Advanced Studies, 31 Fitzwilliam Place, Dublin 2, Ireland*
[7]*Department of Physics, University of Hong Kong, Hong Kong*
[8]*Laboratory for Space Research, The University of Hong Kong, Hong Kong*
[9]*Astronomical Observatory, Volgina 7, PO Box 74 11060 Belgrade, Serbia*
[10]*Department of Astronomy, Faculty of Mathematics, University of Belgrade, Studentski trg 16, 11000 Belgrade, Serbia*
[11]*Isaac Newton Institute of Chile, Yugoslavia Branch*
[12]*Institute for Advanced Research, Nagoya University, Chikusa-ku, Nagoya 464-8601, Japan*
[13]*National Astronomical Observatory of Japan, Mitaka, Tokyo 181-8588, Japan*
[14]*School of Science, University of New South Wales, Australian Defence Force Academy, Canberra, ACT 2600, Australia*
[15]*School of Physical Sciences, University of Adelaide, North Terrace, Adelaide, SA 5005, Australia*
[16]*Department of Physics and Astronomy, University of Calgary, University of Calgary, Calgary, Alberta, T2N 1N4, Canada*
[17]*Space Science Center, Department of Physics, Earth Science and Space Systems Engineering, Morehead State University, Morehead, KY 40351, USA*

Accepted XXX. Received YYY; in original form ZZZ

ABSTRACT

We present a new optical sample of three Supernova Remnants (SNRs) and 16 Supernova Remnant (SNR) candidates in the Large Magellanic Cloud (LMC). These objects were originally selected using deep Hα, [S II] and [O III] narrow-band imaging. Most of the newly found objects are located in less dense regions, near or around the edges of the LMC's main body. Together with previously suggested MCSNR J0541–6659, we confirm the SNR nature for two additional new objects: MCSNR J0522–6740 and MCSNR J0542–7104. Spectroscopic follow-up observations for 12 of the LMC objects confirm high [S II]/Hα emission-line ratios ranging from 0.5 to 1.1. We consider the candidate J0509–6402 to be a special example of the remnant of a possible type Ia Supernova (SN) which is situated some 2° (~1.75 kpc) north from the main body of the LMC. We also find that the SNR candidates in our sample are significantly larger in size than the currently known LMC SNRs by a factor of ~2. This could potentially imply that we are discovering a previously unknown but predicted, older class of large LMC SNRs that are only visible optically. Finally, we suggest that most of these LMC SNRs are residing in a very rarefied environment towards the end of their evolutionary span where they become less visible to radio and X-ray telescopes.

Key words: ISM: supernova remnants – techniques: spectroscopic – (galaxies:) Magellanic Clouds

★ E-mail: m.filipovic@westernsydney.edu.au

1 INTRODUCTION

SNRs play a major role in our understanding of Supernovae (SNe), the interstellar medium (ISM), and the evolution of galaxies as a whole. They are generally divided into two categories according to their progenitors: core-collapse and thermonuclear (type Ia) SNRs. Core-collapse SNRs, as their name suggests, result from massive stars undergoing core collapse. Thermonuclear SNRs are remnants of type Ia SNe occurring when a massive white dwarf in a binary system experiences a runaway thermonuclear fusion reaction resulting in the explosive release of nuclear energy (for a review see e.g. Hillebrandt et al. 2013). These two types of SNe eject heavy elements into the ISM and heat it. SNe create shock waves that compress magnetic fields and efficiently accelerate particles such as energetic cosmic rays observed throughout the Galaxy. Therefore, a complete study of the properties of these two types of SNRs in galaxies can provide an opportunity to understand the origin of cosmic rays, the star formation history and chemical evolution of galaxies.

In general, SNRs are characterised by their simultaneous exhibition of diffuse X-ray emission, their non-thermal radio spectral index, and their high [S II]/Hα ratios as these signatures are produced by high-velocity shocks. We utilise the criteria given in Filipovic et al. (1998b, Sect. 4.1) to establish bona-fide SNRs from SNR candidates. In the simplest form, source X-ray and/or radio confirmation in addition to the high optical [S II]/Hα ratio is necessary for an object to be established as a bona-fide SNR. Otherwise, if a source satisfies only one of these three multi-frequency criteria, we consider it to be an SNR candidate.

Various surveys of SNRs in our Galaxy and nearby galaxies have been carried out at radio, X-ray, Infrared (IR) and optical wavelengths. The first extragalactic SNR candidates were identified in the LMC by Mathewson & Healey (1964) and later confirmed with a combination of radio and optical techniques by Westerlund & Mathewson (1966). To date, a total of 60 SNRs have been confirmed in the LMC with an additional 14 suggested candidates (Maggi et al. 2016; Bozzetto et al. 2017; Maitra et al. 2019). However, sensitivity and resolution limitations severely reduce the effectiveness of the past & present generations of radio and X-ray searches for SNRs in galaxies beyond the Small & Large Magellanic Clouds (MCs) (Goss et al. 1980; Long et al. 1981; Cowan & Branch 1985; Matonick & Fesen 1997; Matonick et al. 1997; Millar et al. 2012; Galvin & Filipovic 2014; Sasaki et al. 2018; Lin et al. 2020; Sasaki 2020). As a result, optical studies have produced the largest number (~1200) of new extra-Magellanic SNR candidates. Optical extragalactic searches for SNRs are mainly done by using an emission line ratio criterion of the form [S II]/Hα > 0.4–0.5 (Mathewson & Clarke 1973; Dodorico et al. 1980; Fesen 1984; Matonick & Fesen 1997; Blair & Long 1997; Dopita et al. 2010b; Lee & Lee 2014; Vučetić et al. 2019b,a, 2018; Lin et al. 2020). This criterion separates shock-ionisation from photoionisation in SNRs from H II regions and Planetary Nebulae (PNe) (Frew & Parker 2010). SNR radiative shocks collisionally excite sulphur ions in the extended recombination region resulting in S^+, hence the larger contribution of [S II] accounting for an increase of the [S II] to Hα ratio. In typical H II regions, sulphur exists predominantly in the form of S^{++}, yielding low [S II] to Hα emission ratios. Ratios from narrow-band imaging are usually verified spectroscopically, since [N II] lines at 6548 and 6584Å can contaminate the Hα images at an unknown and variable level. Spectroscopic observations of such emission nebulae also can provide other evidence of shock heating, such as strong [O I] λ6300 emission, elevated [N II] to Hα with respect to H II regions, or high [O III] electron temperatures, verifying the candidate as being a SNR (Blair et al. 1981, 1982; Long et al. 1990; Smith et al. 1993; Blair & Long 1997). Although somewhat biased as an isolated criterion, this method is proven and a good way of identifying ordinary radiatively cooling SNRs in nearby galaxies. We note that young, Balmer-dominated SNRs (Chevalier et al. 1980) would be missed by this criterion.

The LMC galaxy, the target of this study, lies towards the south ecliptic pole and is in one of the coldest parts of the radio sky, uncontaminated by Galactic foreground emission (Haynes et al. 1991; Reid & Parker 2010). The LMC's position and its known distance of 50 kpc (di Benedetto 2008) makes the LMC arguably an ideal galaxy in which to study SNRs in our Local Group of galaxies. LMC objects can also be assumed to be located at approximately the same distance even with the tilt (inclination) of the LMC at 23° toward the line of sight (Subramanian & Subramaniam 2010). This tilt introduces <10 per cent of additional uncertainty in diameter estimates.

Apart from the above mentioned LMC SNR survey papers, there are a number of studies focusing on particular LMC SNRs, such as N 103B and N 132D. Some recent studies include: Bojičić et al. (2007); Cajko et al. (2009); Crawford et al. (2008, 2010); Crawford et al. (2014a); Bozzetto et al. (2010); Grondin et al. (2012); Bozzetto et al. (2017); de Horta et al. (2012); De Horta et al. (2014); Kavanagh et al. (2013); Brantseg et al. (2014); Kavanagh et al. (2016, 2015c,b,a); Reid et al. (2015); Maggi et al. (2014); Warth et al. (2014); Bozzetto & Filipović (2014); Bozzetto et al. (2015, 2013, 2014a); Bozzetto & Filipović (2014); Bozzetto et al. (2014b, 2012a,b,d,c); Leahy (2017); Ghavamian et al. (2017); Dopita et al. (2018); Maitra et al. (2019); Alsaberi et al. (2019a); Seitenzahl et al. (2019); Leahy et al. (2019); Pennock et al. (2020).

In this paper, we present new optical narrow band imaging data for 19 LMC objects. For 12 of these 19 objects we also have spectroscopic follow-up observations. The nebular lines detected include [O III] 4959/5007Å, [O I] 6300/6364Å, [S II] 6716/6731Å, and hydrogen Balmer lines, Hα, Hβ, Hγ and Hδ. Further, [N II] 6548/6583Å ratio (and line detection) are generally common in SNR spectra, but in the MCs, due to a low abundance of nitrogen (see Dopita 1979; Russell & Dopita 1990; Dopita et al. 2019) these lines are not necessarily detected, or if they are seen they are usually not as intense compared with the same lines of SNRs in the Milky Way (MW) or in other galaxies. These optical lines are common for evolved SNRs, i.e., for remnants whose interiors are in the cooling phase while their shells are merging with the ISM. Compared with old SNRs, younger ones show many more lines in their optical spectra, although they do not share the same spectral classification such as the type of SN explosion and the surrounding ISM. Likewise, in the LMC we notice the existence of non-radiative Balmer dominated and oxygen rich SNRs (see Smith et al. 1991; Vogt & Dopita 2011; Seitenzahl et al. 2018; Vogt et al. 2018) like others discovered in the Galaxy or other galaxies but, somewhat surprisingly, not in M 33 (Long et al. 2010; Lin et al. 2020).

The layout of this paper is as follows: In Section 2 we describe the observations and imaging techniques. In Section 3 we present our results on the 19 LMC objects studied and in Section 4 we investigate the true nature of these objects. Finally, in Section 5 we summarise our findings.

2 OPTICAL AND X-RAY OBSERVATIONS

2.1 Magellanic Cloud Emission Line Survey (MCELS) Observations

We used images from the Magellanic Cloud Emission Line Survey (MCELS; Smith & MCELS Team 1999). These images were taken at the UM/CTIO (University of Michigan) Curtis Schmidt telescope at Cerro Tololo Inter-American Observatory (CTIO). The detector, a Tek 2048 × 2048 CCD with 24 μm pixels, had a scale of 2.3″ per pixel and a resulting angular resolution of approximately 4.6″. The narrowband images were taken with filters centered on the [O III] (λ_c 5008Å, FWHM=50Å), Hα+[N II] (λ_c 6563Å, FWHM=30Å), and [S II] (λ_c 6724Å, FWHM=50Å) emission-lines along with green (λ_c 5130Å, FWHM=155Å) and red (λ_c 6850Å, FWHM=95Å) continuum filters. The optical data were reduced using the IRAF[1] software package for bias subtraction and flat-field correction. The astrometry was derived from stars in the Two Micron All Sky Survey (2MASS) J-band catalog (Skrutskie et al. 2006). The data were flux-calibrated using observations of spectro-photometric standard stars (Hamuy et al. 1994, 1992) and then continuum subtracted. More details about MCELS observations can be found in Points et al. (2019)[2].

In Table 1 we list all 19 objects studied in this paper. In Col. 2 we list the date of the spectroscopic observations for objects listed in Table 2; source name and its central position (RA and DEC) are listed in Cols. 3, 4 and 5; source extent as major and minor axis/diameter are listed in Col. 6 (in arcsec) while in Col. 7 we show the average of major and minor axes converted to parsecs for a distance of 50 kpc; the position angle (PA; Col. 8) is measured from north to east. [S II]/Hα from MCELS in Col. 9 represent the average measured value within the SNR candidate extent after subtracting local noise. Only values > 5σ of the local noise were used and [S II] value provided in Col. 9 is the sum of the 6716Å and 6731Å lines. In Col. 10 we show the number of massive OB stars found within ∼100 pc radius as well as within the object's extent as measured in (Col. 6).

2.2 WiFeS

The Wide-Field Spectrograph (WiFeS; Dopita et al. 2007; Dopita et al. 2010a) was used to obtain the integral field spectra of 12 MCELS selected objects (see Section 3.1 for more details). This integral field unit (IFU) is mounted on the Australia National University (ANU) 2.3-m telescope at the Siding Spring Observatory (SSO). The spectrograph is an image slicer, consisting of a combination of 25 × 1″ wide adjacent slits each 38″ in length to yield an effective 25″× 38″ field of view on the sky.

We performed our WiFeS spectral observation between October 21 and 23, 2017 as well as on September 7, 2019 using the RT560 dichroic as a beam splitter to send light to both the blue and red arms of the spectrograph. However, only the September 7, 2019 observation was done under excellent atmospheric (photometric) conditions. Each observation was 20–50 minutes in length and we used Nod-and-Shuffle techniques as per Dopita et al. (2007). In the blue arm, the medium resolution grating with 708 lines mm^{-1} (B3000; ∼51.7 Å mm^{-1}) was used and for the red arm we used the higher resolution grating of 1200 lines mm^{-1} (R7000; ∼29.0 Å mm^{-1}). According to Dopita et al. (2010a, Table 2), the R7000 grating actually achieves R∼6800 (∼45 km s^{-1}) and the B3000 grating is actually R ∼2900 (∼105 km s^{-1}). At Hα, this means that R7000 grating has a resolution of just under 1 Å (0.965) (Figure A5) and at Hβ B3000 has a resolution of about 1.67 Å.

Our choice of gratings provided overlapping blue and red spectra with a coverage from ∼3400 to 7000 Å. Dopita et al. (2007) and Dopita et al. (2010a) presented the on-telescope end-to-end transmission of the WiFeS spectrograph, including the telescope, atmosphere and detectors. According to this work, the transmission of the R7000 grating (which we used for the red arm observations) at the wavelength of the [S II] sulphur lines is 12.5 per cent lower compared to the transmission at the wavelength of Hα. This transmission correction was applied to all of our relative flux observations of the [S II] lines to Hα.

After the data reduction of the WiFeS observations, which was performed with the PyWiFeS pipeline (Version 0.7.0 e.g. Childress et al. 2014), the final product is a 3D spectral data cube with R.A., Dec and λ as the third dimension. Using a circular or square aperture, summed 1D spectra were extracted from the cube (see example in Stupar et al. 2018). For our sample of obtained cubes, we used circular apertures between 5″ and 10″ positioned at the brightest parts of the SNR filaments to extract 1D spectra (see example in Figure A6 (bottom right)). We used the IRAF splot routine to subtract the sky. The same results were achieved using Starlink Splat routine. [O I] spectral lines at 6300/6363 Å are frequently present in the spectrum of SNRs and are good SNR indicators especially in their young phase. However, they are also present in the spectrum of the night sky. Therefore, distinguishing whether such lines belong to the object or they are from the night sky is of essential importance. To resolve this problem, spectra with the presence of these lines were first checked on 2D data and then their wavelengths were measured. If the wavelengths were exactly 6300/6360 Å, then the lines definitely belong to the night sky and are deleted from the 1D spectra. If the lines were shifted for some 5–6 Å (our usual shift for the LMC) its assumed they originate from the given object, and therefore, the lines are kept in the 1D spectrum. We present details in Section A for all 12 spectroscopically observed objects. Also, Tables 1 and 2 provide aperture positions, relative intensities, and ratios of observed lines.

We note that the intrinsically fainter blue flux of three sources produced very weak blue spectra, so that these three candidates only have data for the red part of spectrum (see Table 2). The blue spectra of other candidates should be taken with the understanding that we have not applied individual reddening corrections. For one object, J0548–6941, we have determined physical fluxes of the observed lines (see Table 2). The fluxes were determined by calibration against the spectrophotometeric standard star LTT1020.

Some line ratios are set by atomic physics. Specifically, the $^1D_2 \rightarrow ^3P$ doublet ratios [O III] 5007/4959Å and [N II] 6583/6548Å must both be ∼2.9 (Acker et al. 1989), which makes measuring the flux of the fainter blue lines ([O III]4959Å and [N II]6548Å) difficult in several cases (e.g. source J0542–7104 (Figure A18) where [O III]4959Å is hardly above the background fluctuations). To avoid adding noise, we measure only the brighter red component of the doublets, and multiply by (1+1/3) to calculate [N II]/Hα and [O III]/Hα ratios.

[1] Image Reduction and Analysis Facility (IRAF) is distributed by the National Optical Astronomy Observatory (NOAO), which is operated by the Association of Universities for Research in Astronomy (AURA) under a cooperative agreement with the National Science Foundation (NSF).
[2] Data can be found in: ftp://ftp.ctio.noao.edu/pub/points/MCELS/LMC/

2.3 *XMM-Newton* data

To search for X-ray emission from our candidate SNRs we created an up-to-date mosaic of all *XMM-Newton* (Jansen et al. 2001) observations available in the LMC area. This included all archival observations that were public up to July 2020, as well as recent observations from projects with author involvement centred within 4° around R.A.(J2000)=$05^h22^m00^s$ and Dec(J2000)=–68° 30′ 00″ (for more detailed descriptions see Maggi et al. 2016; Sturm et al. 2013; Haberl et al. 2012). Observations were processed with *XMM-Newton* science analysis software `SAS` version 17.0.0. We combined the data from the European Photon Imaging Camera, EPIC-pn and EPIC-MOS (Strüder et al. 2001; Turner et al. 2001) and created images in the 0.3–0.7 keV, 0.7–1.1 keV and 1.1–4.2 keV energy bands which were combined with an RGB image. From EPIC-pn we used only single- and double-pixel events (`PATTERN` $\leq$ `4`), and from EPIC-MOS all single- to quadruple-pixel events (`PATTERN` $\leq$ `12`). The X-ray properties of the detected SNRs as revealed by our *XMM-Newton* mosaic will be discussed in future papers including (Kavanagh et al. 2020).

2.4 Magellanic Clouds Photometric Survey

It is very important to understand the type of stellar environment the progenitor of these objects came from. Because of that, we make use of data from the Magellanic Clouds Photometric Survey (MCPS; Zaritsky et al. 2004) in order to construct colour-magnitude diagrams. This way we identify blue stars more massive than ~8 $M_\odot$ within a 100 pc (6.9′) radius of objects selected in this study. This allows us to see the prevalence of early-type stars close to the remnant candidates.

3 RESULTS

From careful examination of the MCELS images, we select 19 LMC objects and classify them as potential new SNR candidates. We base this classification on their morphological characteristics as well as their [S II]/Hα ratios (see Table 1 and Figure 1 for their positions across the LMC field). We include in our sample MCSNR J0541–6659, which was previously classified as an SNR by Grondin et al. (2012) using X-ray observations (Figure A17) but never confirmed spectroscopically.

Figures A1, A3, A4, A5, A6, A8, A9, A11, A16, A18, A19 and A21 show the 12 spectroscopically studied LMC objects with their associated WiFeS spectra and the MCELS images (namely: Hα, [S II] [O III] and the ratio [S II]/Hα).

In Figures A2, A7, A12, A13, A14, A15 and A20 we show seven additional MCELS objects, which we propose as new LMC SNRs or SNR candidates. However, we have not yet obtained any spectroscopic follow-up observations of these objects. Three of these seven objects are detected in X-rays which additionally support their classification as SNRs. Because of the lack of spectroscopic confirmation as well as the lack of confirmed detections at other frequencies, we assign a lower confidence classification (as SNR candidates) for the four remaining sources in this sample of seven objects.

3.1 Optical Identification of Newly Selected LMC objects

It is well established that the most reliable SNR diagnostic of optical spectral observations is the ratio of the [S II]/Hα lines. This confirms the presence of radiative shock(s) and a ratio of >0.4 suggests an SNR origin. However, we note that [S II]/Hα can also reach 0.4 (and higher) in ionisation fronts as well as in diffuse gas ionised by a diluted UV flux. A good example is NGC 7793 where the optical search for SNRs was severely complicated by extensive diffuse [S II]/Hα photoionised gas throughout the galaxy and rises well above the value of 0.4 (Blair & Long 1997). The [S II]/Hα ratio alone is thus not sufficient to robustly confirm an SNR classification as X-ray and/or radio confirmation is also needed. All discrete objects in Table 2 satisfy these optical criteria indicating their possible SNR nature. The shell structure of the observed sample, clearly seen on MCELS images in Hα, [S II] and [O III] light, also supports the fact that these objects are excellent SNR candidates.

Additionally, the existence of [O III] emission that is localised to a thin shell is another indicator that the source is indeed of SNR origin as it traces out the radiative cooling zone. But if it is extended, especially in the inner part of the nebula, it is more typical of a high (photo-)ionisation nebula, and argues against an SNR interpretation.

In Figure 2 we show the ratio of the [S II]λ6716 and [S II]λ6731 lines versus log (Hα/([S II]λ6716+[S II]λ6731)) for the sample of our 12 spectroscopically studied LMC objects (following Sabbadin et al. (1977)). This diagram maps the locations in this graph that would be occupied by H II regions, SNRs and PNe. This diagram is based on Galactic SNRs, H II regions and PNe and is representative of nearby galaxies such as the LMC.

Using our high resolution spectroscopic observations, we find one of the initially selected SNR candidates having an elevated [S II]/Hα ratio which is just out of the range expected for SNRs (J0549–6633; marked in red in Figure 2). We still classify this object, though, as a somewhat more likely SNR candidate then a (super)bubble (see Appendix A19). The rest of our sample nicely fits in the group of older SNRs because of the higher ratio of sulphur lines – just as it is predicted by Sabbadin et al. (1977). This is in agreement with the findings of Long et al. (2018) for M 33 SNRs where some very large shells with elevated [S II] emission were seen. Recently, Fesen et al. (2020) also found a new large optically visible but radio and X-ray faint Galactic SNR.

Sabbadin et al. (1977) also use a diagram of Hα/[N II] vs. Hα/[S II] (in log scale, their Fig. 2). H II regions have smaller [N II]/Hα ratios than SNR which adds another tool to separate these two group of sources. A very low value for our candidates J0502–6739 (looks more like H II region) and J0542–7104 casts some doubts on their classification as SNR candidates from the spectroscopic point of view. Certainly, Sabbadin et al. (1977) estimates were for MW objects, and as we mentioned earlier (see Section 1) the LMC has nitrogen deficiency.

In Table 2 we also show the ratio of [N II]/Hα lines with a median (for this sample) of ~0.27 (SD=0.10). This is a somewhat lower than expected ratio compared to Galactic SNRs, but it is acceptable because of the overall lower nitrogen abundance of the LMC compared to the MW (see also Reid et al. 2015). Depending on the local abundance in the Galaxy (see example in Stupar et al. 2018), this ratio for SNRs could vary by as much as a factor of ~2 (or even more). In the blue part of the spectrum, we detected the oxygen line [O III]λ5007 in six SNR candidates (MCSNR J0541–6659, J0444–6758, J0455–6830, J0517–6757, MCSNR J0542–7104 and J0548–6941). The presence of this line suggests that the shock velocity is between 80 km s^{-1} and 140 km s^{-1} because a speed of over 140 km s^{-1} would produce more Hβ emission than the oxygen line which becomes relatively weak. However, spectra of these six putative remnants (and their relative intensities as listed in Table 2) show a rather strong [O III]λ5007 line. The exception is again

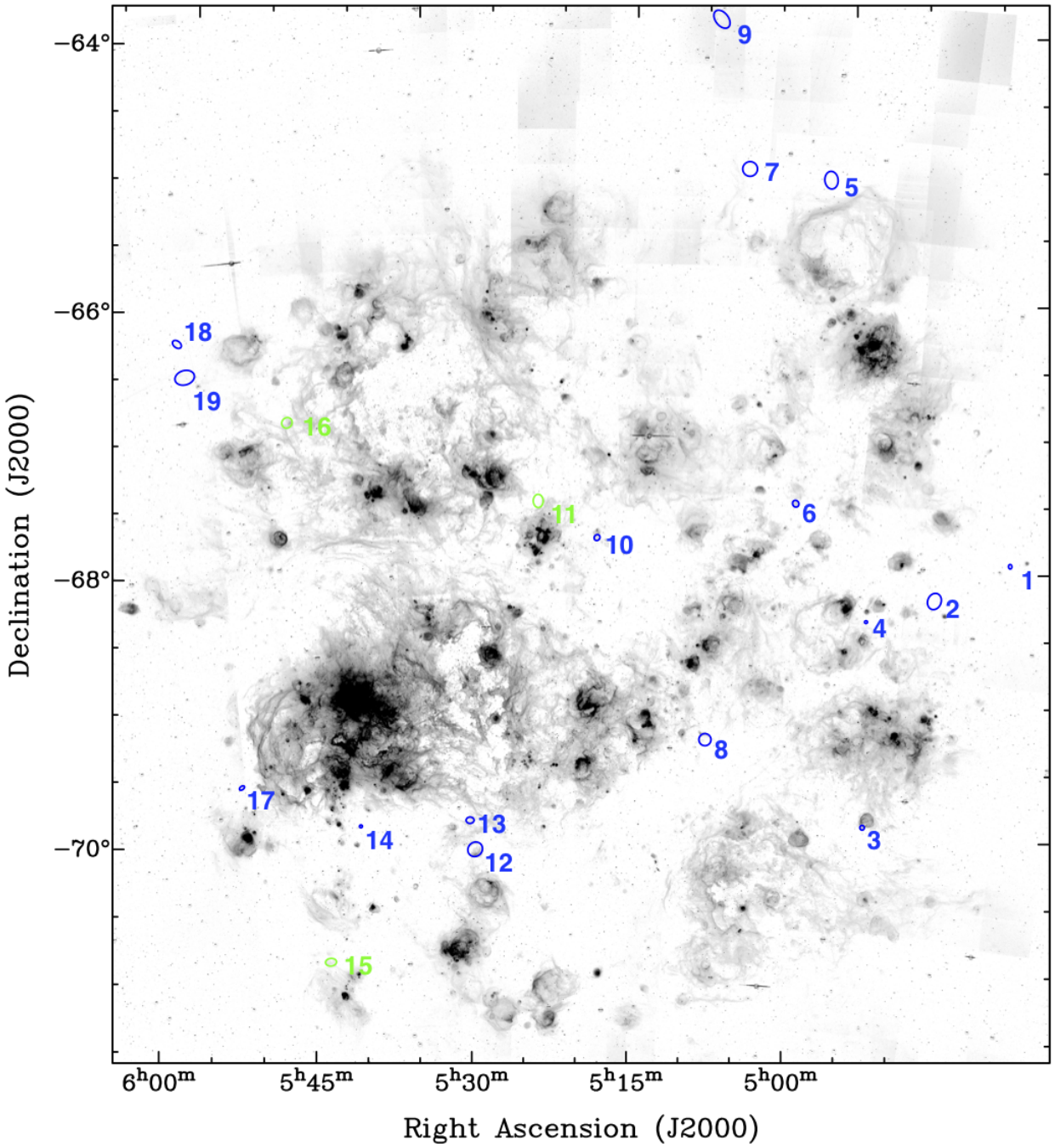

Figure 1. The positions of 16 new SNR candidates in the LMC are marked in blue. Previously classified X-ray SNR — MCSNR J0541–6659 and here classified MCSNR 0522–6740 and MCSNR J0542–7104 are marked in green colour with corresponding numbers as in Table 1 (Col. 1). Background (grey scale) image is MCELS Hα.

MCSNR J0541–6659 where Hβ is much stronger than the usually strong [O III]λ5007 line. The last column in Table 2 presents electron densities for the given sample calculated on the basis of the [S II]λ6716/[S II]λ6731 line ratios with an assumed electron temperature of 10 000 K. Assessment of values in this column suggests an overall older SNR population including five objects that are at a low electron density (e.g. out of the electron density function; marked with LDL (low density limit) in the last column of Table 2).

While these spectroscopic results suggest that our newly selected objects are SNRs, we cannot take that as the final classification. Apart from a confirmation at other frequencies (Filipovic et al. 1998b; Bozzetto et al. 2017), a question arises from the fact that the shell structure and the ratio of sulphur lines with Hα (e.g. the shock) are not seen only in SNRs. For example, a Wolf Rayet (WR) star nebula is also a source of nebulously where shocks are observed as they are released from a WR star. However, the sizes of WR shells are certainly smaller compared to SNRs. For our sample of sources studied here, the indication of a possible WR star nebula can be

Table 1. The main characteristics of the 19 LMC objects in this study.

No.	Obs. Date	Name	RA (J2000) (h m s)	DEC (J2000) (° ′ ″)	$D_{maj} \times D_{min}$ (″)	D_{av} (pc)	PA (°)	MCELS [S II]/Hα	OB stars No.	Figure No.
(1)	(2)	(3)	(4)	(5)	(6)	(7)	(8)	(9)	(10)	(11)
1	22/10/2017	0444–6758	04 44 27.8	–67 58 13.1	124 × 92	25.9	80	0.7	1/0	A1
2	23/10/2017	0450–6818	04 50 12.4	–68 18 04.8	454 × 366	98.8	105	0.8	1/1	A2
3	not obs.	0454–7003	04 54 19.1	–70 03 30.5	129 × 121	30.3	80	0.8	18/0	A3
4	21/10/2017	0455–6830	04 55 36.8	–68 30 34.6	80 × 78	19.1	170	0.9	18/0	A4
5	22/10/2017	0500–6512	05 00 58.5	–65 12 15.3	480 × 360	100.8	80	0.8	0/0	A5
6	22/10/2017	0502–6739	05 02 02.5	–67 39 31.3	190 × 168	43.3	60	0.6	18/2	A6
7	not obs.	0506–6509	05 06 51.7	–65 09 16.6	402 × 398	97.0	170	0.6	—	A7
8	22/10/2017	0508–6928	05 08 31.8	–69 28 29.8	330 × 330	80.0	0	0.7	7/2	A8
9	22/10/2017	0509–6402	05 09 16.1	–64 02 11.3	556 × 350	106.9	50	0.7	—	A9
10	23/10/2017	0517–6757	05 17 51.1	–67 57 46.0	170 × 150	38.7	130	0.7	17/0	A11
11	not obs.	0522–6740	05 22 32.4	–67 40 56.0	360 × 270	75.6	90	1.0	7/1	A12
12	not obs.	0528–7017	05 28 46.0	–70 17 56.8	416 × 380	96.4	140	0.9	13/4	A13
13	not obs.	0529–7004	05 29 05.9	–70 04 40.6	216 × 174	47.0	0	1.0	12/0	A14
14	not obs.	0538–7004	05 38 47.2	–70 04 15.8	80 × 80	19.4	0	0.8	2/0	A15
15	23/10/2017	0541–6659	05 41 51.5	–66 59 02.8	300 × 272	69.2	0	0.5	18/2	A16
16	23/10/2017	0542–7104	05 42 37.9	–71 04 13.6	300 × 210	60.8	0	0.7	1/0	A18
17	07/09/2019	0548–6941	05 48 49.1	–69 41 18.3	156 × 95	29.5	150	0.6	4/0	A19
18	not obs.	0549–6618	05 49 30.1	–66 18 15.9	270 × 180	53.4	45	1.0	0/0	A20
19	23/10/2017	0549–6633	05 49 14.5	–66 33 43.1	540 × 390	111.2	170	1.4	0/0	A21

Table 2. The relative fluxes and most important line ratios (in the red arm) of observed emission lines for 12 LMC objects. To extract spectra from WiFeS cube we used apertures between 5 and 10 arcsec. LDL (Column 15) stands for "low density limit". Also, J0548–6941 is the only source with physical (calibrated) flux values for which the spectroscopic standard star LTT1020 was used. All other objects are with relative flux (counts). All fluxes for J0548–6941 in units of erg cm^{-2} s^{-1}Å^{-1}. Errors in flux estimates for blue end of the spectra are in order of 17–19 per cent, and for red arm observations 23–25 per cent what can be expected for lower signal-to-noise for the higher resolution spectra, while dispersion errors are as in Dopita et al. (2007); Dopita et al. (2010a); Childress et al. (2014). [N II] and [S II] used in Columns 13 and 14 for the ratios relative to Hα are the sum of the doublet lines. The [S II]6548Å line flux is derived from that of the 6563Å line (see Sect. 2.2).

Object Name	Hδ 4101Å	Hγ 4342Å	Hβ 4861Å	[Fe II] 4890Å	[O III] 5007Å	[O I] 6300Å	Hα 6563Å	[N II] 6583Å	[S II] 6716Å	[S II] 6731Å	[S II]/[S II] 6716Å/6731Å	[N II]/Hα	[S II]/Hα	Elect. den. (cm^{-3})
(1)	(2)	(3)	(4)	(5)	(6)	(7)	(8)	(9)	(10)	(11)	(12)	(13)	(14)	(15)
J0444–6758			83		1085		1103	277	446	286	1.5	0.33	0.67	LDL
J0450–6818						302	1101	212	523	364	1.4	0.26	0.80	26.5
J0455–6830			100		580		1824	624	1192	838	1.4	0.46	1.10	26.5
J0500–6512							1111	152	540	359	1.5	0.18	0.81	LDL
J0502–6739		588	1563			180	5196	536	1692	1180	1.4	0.14	0.55	26.5
J0508–6928	631	1270	4260			533	22952	5073	9906	6628	1.5	0.29	0.72	LDL
J0509–6402						280	1107	224	461	373	1.2	0.27	0.75	29.8
J0517–6757		82	1420		2078	488	6284	1531	2447	1871	1.3	0.32	0.69	26.5
J0541–6659	1281	3805	12957		5944		19692	3045	5672	4120	1.4	0.21	0.50	26.5
J0542–7104			30		101	331	3688	113	1835	1198	1.5	0.04	0.82	LDL
J0548–6941	2.5×10^{-16}		1.1×10^{-15}	3.1×10^{-16}	1.5×10^{-15}		1.3×10^{-15}	2.5×10^{-16}	3.7×10^{-16}	2.4×10^{-16}	1.5	0.26	0.47	LDL
J0549–6633						731	1989	400	1618	1129	1.4	0.27	1.38	26.5

also rejected as none of our sources can be found in the recent comprehensive survey of WR stars in LMC (Neugent et al. 2018).

Lasker (1977) demonstrated that some LMC shell nebulae would have [S II] (6716, 6731Å) strengths of the same order as Hα as well as expansion velocities of ~30 km s^{-1}. He argued that the ionisation is radiative and that the additional heating required to explain the strong [S II] is furnished by shocks. In summary, it is challenging to determine whether these shocks are driven by SN blasts or by stellar winds. A number of examples can be seen across the LMC in objects such as N 185, N 186 and N 70 (Oey et al. 2002; De Horta et al. 2014). However, some of the objects (for example N 9; Bozzetto et al. 2017) from the Lasker (1977) sample were later confirmed as a true SNRs. Essentially, if any of these large shells are driven by stellar winds, one would expect to find some massive (OB) stars in the vicinity of these objects to create those stellar winds. This would be a most straightforward way to distinguish one from the other.

Similar to SNRs and WR star nebula, (super)bubbles also show shell structure as well as shocked radiative spectra. But in most cases, inside the shell, the material is far less dense (particularly seen in Hα light) and propelled by the fast stellar winds because of the loss of energy from a massive star (see Chu 2008). (Super)bubbles are also usually associated with a massive stellar population. MCELS images of the whole sample (except MCSNR J0542–7104; see later

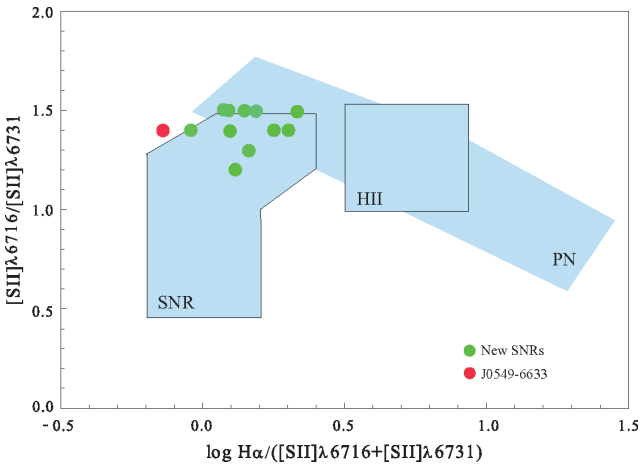

Figure 2. Ratio of [S II]λ6716 and [S II]λ6731 lines versus log Hα/[S II]λ6716+[S II]λ6731 for the sample of our 12 spectroscopically observed LMC objects presented in this paper. 11 objects from Table 2 fit in the designated area of SNRs while the object marked as a red dot (J0549–6633; Section A19) is slightly out. Noticeably, all these objects occupy the area suggested for older remnants as predicted by Sabbadin et al. (1977).

discussion) do not show any obvious dense material inside the shells. Thus, for our sample of objects, a classification as a (super)bubble is somewhat unlikely. One, though, should always consider a possible confusion with other nearby objects such as H II regions (Bojičić et al. 2007).

As radio-continuum objects, SNRs are well known by their non thermal emission seen at different radio frequencies. Our search for radio emission from the new optically selected sample of SNR candidates failed to detect any such emission. We searched all present-day radio surveys including the latest and most sensitive Australian Square Kilometre Array Pathfinder (ASKAP) survey of the LMC at 888 MHz (Filipović et al., in prep). Existing X-ray surveys of the LMC such as from the *RÖntgen SATellite (ROSAT)* (Filipovic et al. 1998a) and *XMM-Newton* (Maggi et al. 2016), with their noticeably limited area coverage compared to radio and optical data, likewise did not show any signs of SNR-like emission except for MCSNR J0542–7104 ([HP99] 1235; Section A16) as reported in Kavanagh et al. (2020; in prep.), J0454–7003 (Section A3), J0529–7004 ([HP] 1077; Section A13) and MCSR J0522–6740 (Section A11).

We did not find any infrared emission from any object in our sample (Lakićević et al. 2015, also see;). SNRs are often connected with infrared emission from the time of a SN explosion where it is suggested that the dust grains are formed within the expanding and cooling ejecta (see more details in Williams & Temim 2017; Lakićević et al. 2015). During the later SNR phase, the source of infrared emission is shock-heated dust. Usually younger SNRs emit in mid-infrared wavelengths even though some recent observations of the Small Magellanic Cloud (SMC) remnant and Pulsar Wind Nebulae (PWN) DEM S5 suggest otherwise (Alsaberi et al. 2019b). In older SNRs, which is the most likely case for our sample studied here, the dominant radiation is optical (see our spectra) and UV radiation where cooled gas in a post-shock environment with low radiative shock speed (about 100 km s^{-1}) is observed. This cooler emission is in the far infrared and could explain why we saw no infrared emission in our sample of evolved remnants.

From these 19 SNR candidates, MCSNR J0522–6740, MCSNR J0541-6659 and MCSNR J0542–7104 are confirmed SNRs (Appendix A11, A15 and A16). The remaining 16 objects studied here are all excellent new SNR candidates.

4 DISCUSSION

We found that our new LMC SNRs and SNR candidates are larger in comparison to other confirmed LMC SNRs (see Table 1) but only after excluding three smaller size objects: J0444–6758, J0455–6830 and J0538-7004. Those three were most likely previously undetected SNRs due to the confusion with larger H II regions.

To calculate the physical diameter distribution for these 16 SNRs and SNR candidates the kernel smoothing procedure described in Maggi et al. (2019) is applied (Figure 3). For comparison, the same procedure is also applied to the sample of 59 SNRs from Bozzetto et al. (2017, Fig. 8). It is evident that the sample diameters from this work have values almost two times larger (with correspondingly higher uncertainties) for the stated distribution parameters, while the smoothing bandwidth differs by about 15 per cent. We find that the average size of the 16 SNRs and SNR candidates to be 71±14 pc (SD=27). Bozzetto et al. (2017) found that the LMC SNR population exhibits a mean diameter of 39±4 pc for the earlier confirmed 59 LMC SNR. Our discovery of these 16 large LMC SNR candidates nicely agree with the Bozzetto et al. (2017) prediction that the present sample with sizes D>40 pc is incomplete, leaving room for a future detection of mainly large (and older) LMC SNRs (such as these 16). We also note that our new SNR size distribution is much closer to the SMC sample (Maggi et al. 2019) which is smaller in number but noticeably more complete. The sample from this work shows indications of the secondary distribution peak at $\approx$ 45 pc, which corresponds to the peak of the distribution for the sample from Bozzetto et al. (2017).

As mentioned earlier, Fesen et al. (2020) found a large, new optically visible but radio and X-ray faint Galactic SNR – G107.0+9.0 with an estimated size of ~75 – 100 pc, an advanced age of ~100 000 yrs and well above the Galactic plane (250–300 pc). However, most of its large shell is not as high in [S II]/Hα ratio as the objects studied here. Still, one selected location where Fesen et al. (2020) obtained a spectrum does contain an elevated ratio, apparently from a relatively slow but radiative shock in an isolated emission knot. This provokes an interesting question: what would G107.0+9.0 look like if it were at the distance of the LMC? To start with, if it is anywhere close to the 30 Doradus region it would most likely be indistinguishable from the local environment which is crowded with bright H II region filaments. Or at best, we would see something similar to J0528–7017 which we study here. But, if G107.0+9.0 is positioned well outside the LMC we would most likely see it to be similar to our J0450–6818, J0500–6512, J0506–6509, J0508–6928, J0522–6740, MCSNR J0542–7104 or J0549–6618.

As in Bozzetto et al. (2017), we investigate the spatial distribution and local environment of these 19 new LMC SNRs and SNR candidates in relation to the H I peak temperature map from Kim et al. (1998). Most of these new SNR candidates (15 out of 19) are positioned near or around the edges of the LMC's main body, in obviously less dense regions.

As argued by Long et al. (2018), the majority of the objects with high [S II]/Hα line ratios (>0.4) are indeed SNRs, but the distinction between H II regions and SNRs becomes far less obvious at low surface brightness, and additional criteria, such as X-ray or radio continuum detection, are needed. We also note that these outer regions of the LMC lack good X-ray coverage, and there-

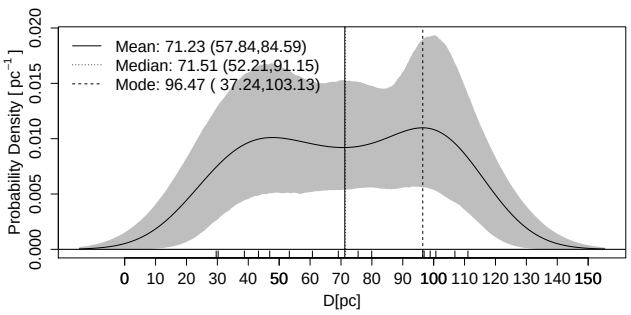

Figure 3. Smoothed diameter distribution for the samples of 16 selected and here studied LMC SNRs. The smoothing procedure and 95 per cent bootstrap confidence intervals are calculated as described in Maggi et al. (2019). The grey lines present a 95 per cent confidence interval around the smoothed distribution. The obtained value for the

smoothing bandwidth h is also designated on the plot.

fore confirmation of the true nature of these objects cannot yet be made. The recent *XMM-Newton* detection of MCSNR J0542–7104 (Kavanagh et al. 2020; in prep) and MCSNR J0522–6740 which is classified here, show that the SNR candidacy of our selected object sample is solid. Further, we report here the detection of diffuse soft X-ray emission from three of our objects with *XMM-Newton* (J0454–7003, MCSNR J0522–6740 and J0529–7004). We note that in all three cases the X-ray emission is more centrally peaked. However, the short exposures and large off-axis angles of the observations do not allow a more detailed analysis of their faint X-ray emission. Despite the lack of deeper coverage we manage to classify one of these three sources (MCSNR J0522–6740; see Appendix A11) as a new bona-fide SNR.

As discussed by Lopez & Fesen (2018), the environment and the surrounding medium influences SNR morphology. More specifically, the progenitors of Core Collapse (CC) SNe have short main-sequence lives (3 – 50 Myr) and their explosions are expected to occur within or near the dense media from which the massive stars formed. The mean H I column density in the direction of the 59 confirmed and 15 candidate remnants, from Bozzetto et al. (2017), was estimated to be $\sim 2 \times 10^{21}$ atoms cm^{-2} (with a SD=$1{\times}10^{21}$ atoms cm^{-2}). Our sub-sample of 15 new SNR objects (excluding three smaller SNR candidates and bona-fide SNR MCSNR J0541–6659 as they are possibly embedded in H II regions) show a marginally lower environmental density of $\sim 1.8 \times 10^{21}$ atoms cm^{-2} (SD=$1.3{\times}10^{21}$ atoms cm^{-2}). Therefore, we find no significant difference in the H I environment in which our new sub-sample of the LMC SNR candidates resides and evolves.

Maggi et al. (2016) argue that the relatively large population of the LMC SNRs could be a product of type Ia SNe, as we also argued for the distant candidate J0509–6402 studied here and new bona-fide SNR MCSNR J0542–7104, although it should be considered with caution. We emphasise that the H I environment around SNR candidates studied here is not vastly different from the previously established LMC SNRs sample as shown above. But the low number of massive (OB) stars within the boundaries of the SNR candidates may favour an SN type Ia origin. However, this should be taken only as indirect evidence.

The larger physical size of our SNR candidates sample could indicate their possibly older age and more evolved phase as also observed for a number of Galactic SNRs by Stupar et al. (2008), Fesen et al. (2019) and recently Fesen et al. (2020). However, one should be very careful comparing our results from the MCs sample with MW SNRs because close to the Galactic plane the absorption is sufficient to absorb most X-ray emission for any but the young SNRs (emitting above 1 or 2 keV). When comparing with other waveband surveys such as X-ray *Chandra* or *XMM-Newton* and ASKAP/Australia Telescope Compact Array (ATCA) radio images, we find that these new LMC SNR candidates are seen almost exclusively in the optical wavelengths. However, the exception are three confirmed SNRs (MCSNR J0522–6740, MCSNR J0541–6659 and MCSNR J0542–7104) as well as two candidates (J0454–7003 and J0529–7004) which can be detected in the X-ray surveys. This could potentially imply that we are discovering a previously unknown class of large and predominantly optically visible LMC SNRs. We suggest that these SNRs are mainly residing in a very rarefied environment and are likely relatively old (>20 kyr). This would make them less visible to the present generation of radio and X-ray telescopes.

Evidently, larger (and older) remnants seen mostly in optical wavebands are radio and X-ray quiet since they are in the last dissipation phase and they almost blend with the ISM. Their emission in those domains are likely to cease because of radiative cooling and the decrease of their strong magnetic fields to the level of the galactic background. SNR non-thermal emission ends because of this dissipation and therefore is not detectable (Stupar et al. 2008).

SNRs in free expansion and Sedov phases of evolution (defined by the non-radiative shocks) can not be easily detected by the [S II]/Hα method. In these phases, [S II] emission of SNR is at best small because they are usually mixed within the local ISM (or H II regions). Even for the nearby galaxies such as the LMC, this causes a selection effect that adversely affects the detection of objects such as SNRs. In the early phases of their evolution, SNRs are mainly detected by radio and X-ray observations and (for SN type Ia) in optical bands only by Balmer lines (Lin et al. 2020). H II regions are also detected by Balmer lines and therefore to rely only on optical detection will not be sufficient especially for SNRs in the free expansion and Sedov phases. In the radiative phases of evolution, SNRs are usually not easily detected in radio and X-rays if they are distant and evolve in a low density environment. In general, this is one of the major detection challenges for distant extragalactic SNR samples where the instrumental sensitivity selection effects dominates the construction of a complete SNR sample.

We follow (and update) the Bozzetto et al. (2017) comparison of multi-frequency emission from known SNRs (60; including one from Maitra et al. (2019)) and SNR candidates (32 including 18 from this work and 14 from Bozzetto et al. (2017) as Maitra et al. (2019) confirmed MCSNR J0513–6731) in the LMC. Also, we plot a Venn diagram (Figure 4) that summarises the number of SNRs (and candidates) exhibiting emission in different electromagnetic domains. We emphasise that the lack of detected emission does not always mean that the remnant does not emit such radiation. Alternatively, it may indicate that the emission is below the sensitivity level of current surveys. Importantly, there are examples of SNRs such as the SMC SNR HFPK 334 (Crawford et al. 2014b; Joseph et al. 2019; Maggi et al. 2019), SMC IKT 23, MCSNR J0528–6713 (Crawford et al. 2010) or the Galactic Vela Jr SNR (Filipović et al. 2001; Stupar et al. 2005; Fukui et al. 2017; Maxted et al. 2018) that could not be identified in optical frequencies despite extensive searches.

Various optical, radio and X-ray SNR detection methodologies have biases as can be seen in our Venn diagrams (Figure 4 and (Bozzetto et al. 2017)). If there are no biases one would expect that all SNRs from one sample would converge to common intersection

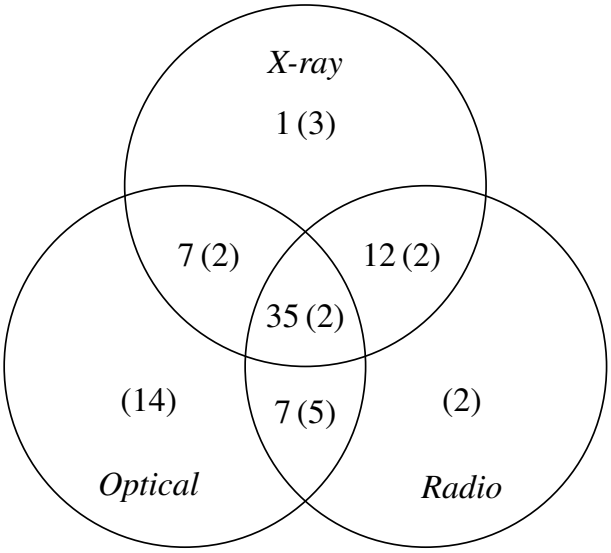

Figure 4. A Venn diagram showing 62 confirmed LMC SNRs (including three from this work). We also show (in brackets) the previously known 14 SNR candidates from Bozzetto et al. (2017) and the here proposed 16 new SNR candidates in different electromagnetic domains.

of all three circles of the Venn diagrams, with zero SNRs in different observational wavebands.

5 CONCLUSIONS

We study previously selected MCSNR J0541–6659 and confirm its optical SNR signature. We also classify previously unknown MCSNR J0522–6740 and MCSNR J0542–7104 as new LMC SNRs. Finally, 16 other objects studied here for the first time are good SNR candidates that require further studies to confirm their real nature.

In total, this work adds two new bona-fide SNRs to the list of 60 previously confirmed SNRs and 16 new SNR candidates to the list of 14 previously known in the LMC as per Bozzetto et al. (2017) and Maggi et al. (2019), respectively. We believe the reason as to why these SNR candidates were not detected previously is due to the fact they are mainly positioned in the outer field of the LMC where they can only be detected because of the high sensitivity of MCELS. This could mean we are looking at an unknown (but predicted) class of large and only (at this stage) optically visible SNRs. The 16 new SNRs and SNR candidates studied here have an average size of 71 pc which is almost a factor of 2 larger (71 pc vs. 39 pc) than those in Bozzetto et al. (2017). We suggest that this sample is older and perhaps in the last evolutionary phase of their lives.

J0509–6402 is a prime candidate of type Ia SNR situated 2° north of the LMC, in a field where low surface brightness stellar population from the LMC extend much further than the main (gaseous) body (Mackey et al. 2018). Two other candidates (J0454–7003 and J0529–7004) were found that exhibit X-ray emission but only further studies can confirm their real nature.

ACKNOWLEDGEMENTS

The MCELS was funded through the support of the Dean B. McLaughlin fund at the University of Michigan and through NSF grant 9540747. M.S. acknowledges support by the Deutsche Forschungsgemeinschaft through the Heisenberg professor grants SA 2131/5-1 and 12-1. We thank You-Hua Chu for her comments and suggestions. B.V. was funded by the Ministry of Education, Science and Technological Development of the Republic of Serbia through the contract number 451-03-68/2020-14/200002. Lastly, we thank the referee for their very constructive and insightful comments and suggestions.

DATA AVAILABILITY

The data underlying this article will be shared on reasonable request to the corresponding author.

REFERENCES

Acker A., Köppen J., Samland M., Stenholm B., 1989, The Messenger, 58, 44
Alsaberi R. Z. E., et al., 2019a, Ap&SS, 364, 204
Alsaberi R. Z. E., et al., 2019b, MNRAS, 486, 2507
Blair W. P., Long K. S., 1997, ApJS, 108, 261
Blair W. P., Kirshner R. P., Chevalier R. A., 1981, ApJ, 247, 879
Blair W. P., Kirshner R. P., Chevalier R. A., 1982, ApJ, 254, 50
Bojičić I. S., Filipović M. D., Parker Q. A., Payne J. L., Jones P. A., Reid W., Kawamura A., Fukui Y., 2007, MNRAS, 378, 1237
Borkowski K. J., Hendrick S. P., Reynolds S. P., 2006, ApJ, 652, 1259
Bozzetto L. M., Filipović M. D., 2014, Ap&SS, 351, 207
Bozzetto L., Filipović M., Crawford E., Bojičić I., Payne J., Mendik A., Wardlaw B., De Horta A., 2010, Serbian Astronomical Journal, pp 43–49
Bozzetto L. M., Filipović M. D., Crawford E. J., Payne J. L., de Horta A. Y., Stupar M., 2012a, Rev. Mex. Astron. Astrofis., 48, 41
Bozzetto L. M., Filipović M. D., Crawford E. J., De Horta A. Y., Stupar M., 2012b, Serbian Astronomical Journal, 184, 69
Bozzetto L. M., Filipović M. D., Urosevic D., Crawford E. J., 2012c, Serbian Astronomical Journal, 185, 25
Bozzetto L. M., et al., 2012d, MNRAS, 420, 2588
Bozzetto L. M., et al., 2013, MNRAS, 432, 2177
Bozzetto L. M., et al., 2014a, MNRAS, 439, 1110
Bozzetto L. M., Filipović M. D., Urošević D., Kothes R., Crawford E. J., 2014b, MNRAS, 440, 3220
Bozzetto L. M., Filipović M. D., Haberl F., Sasaki M., Kavanagh P., Maggi P., Urosevic D., Sturm R., 2015, Publication of Korean Astronomical Society, 30, 149
Bozzetto L. M., et al., 2017, The Astrophysical Journal Supplement Series, 230, 2
Brantseg T., McEntaffer R. L., Bozzetto L. M., Filipović M., Grieves N., 2014, ApJ, 780, 50
Cajko K. O., Crawford E. J., Filipović M. D., 2009, Serbian Astronomical Journal, 179, 55
Chevalier R. A., Kirshner R. P., Raymond J. C., 1980, ApJ, 235, 186
Childress M. J., Vogt P. A., Nielsen J., Sharp R. G., 2014, Ap&SS, 349, 617
Chu Y. H., 2008, IAU Symposium, 250, 341
Cowan J. J., Branch D., 1985, ApJ, 293, 400
Crawford E. J., Filipović M. D., de Horta A. Y., Stootman F. H., Payne J. L., 2008, Serbian Astronomical Journal, 177, 61
Crawford E. J., Filipović M. D., Haberl F., Pietsch W., Payne J. L., de Horta A. Y., 2010, A&A, 518, A35
Crawford E. J., Filipović M. D., McEntaffer R. L., Brantseg T., Heitritter K., Roper Q., Haberl F., Urošević D., 2014a, The Astronomical Journal, 148, 99
Crawford E. J., Filipović M. D., McEntaffer R. L., Brantseg T., Heitritter K., Roper Q., Haberl F., Urošević D., 2014b, AJ, 148, 99
De Horta A. Y., et al., 2014, AJ, 147, 162
Dodorico S., Dopita M. A., Benvenuti P., 1980, Astronomy and Astrophysics Supplement Series, 40, 67

Dopita M. A., 1979, Australian Journal of Physics, 32, 123
Dopita M., Hart J., McGregor P., Oates P., Bloxham G., Jones D., 2007, Astrophysics and Space Science, 310, 255
Dopita M., et al., 2010a, Ap&SS, 327, 245
Dopita M. A., et al., 2010b, ApJ, 710, 964
Dopita M. A., Vogt F. P. A., Sutherland R. S., Seitenzahl I. R., Ruiter A. J., Ghavamian P., 2018, ApJS, 237, 10
Dopita M. A., Seitenzahl I. R., Sutherland R. S., Nicholls D. C., Vogt F. P. A., Ghavamian P., Ruiter A. J., 2019, AJ, 157, 50
Fesen R. A., 1984, ApJ, 281, 658
Fesen R. A., Neustadt J. M. M., How T. G., Black C. S., 2019, MNRAS, 486, 4701
Fesen R. A., et al., 2020, MNRAS,
Filipovic M. D., et al., 1998a, A&AS, 127, 119
Filipovic M. D., Haynes R. F., White G. L., Jones P. A., 1998b, A&AS, 130, 421
Filipović M. D., Jones P. A., Aschenbach B., 2001, in Holt S. S., Hwang U., eds, American Institute of Physics Conference Series Vol. 565, Young Supernova Remnants. pp 267–270, doi:10.1063/1.1377103
Frew D. J., Parker Q. A., 2010, Publ. Astron. Soc. Australia, 27, 129
Fukui Y., et al., 2017, The Astrophysical Journal, 850, 71
Galvin T. J., Filipovic M. D., 2014, Serbian Astronomical Journal, 189, 15
Ghavamian P., Seitenzahl I. R., Vogt F. P. A., Dopita M. A., Terry J. P., Williams B. J., Winkler P. F., 2017, ApJ, 847, 122
Goss W. M., Ekers R. D., Danziger I. J., Israel F. P., 1980, MNRAS, 193, 901
Grondin M.-H., et al., 2012, A&A, 539, A15
Haberl F., Pietsch W., 1999, A&AS, 139, 277
Haberl F., et al., 2012, A&A, 545, A128
Hamuy M., Walker A. R., Suntzeff N. B., Gigoux P., Heathcote S. R., Phillips M. M., 1992, PASP, 104, 533
Hamuy M., Suntzeff N. B., Heathcote S. R., Walker A. R., Gigoux P., Phillips M. M., 1994, PASP, 106, 566
Haynes P. H., McIntyre M. E., Shepherd T. G., Marks C. J., Shine K. P., 1991, Journal of the Atmospheric Sciences, 48, 651
Henize K. G., 1956, ApJS, 2, 315
Hillebrandt W., Kromer M., Röpke F. K., Ruiter A. J., 2013, Frontiers of Physics, 8, 116
Jansen F., et al., 2001, A&A, 365, L1
Joseph T. D., et al., 2019, MNRAS, 490, 1202
Kavanagh P. J., et al., 2013, A&A, 549, A99
Kavanagh P. J., Sasaki M., Bozzetto L. M., Filipović M. D., Points S. D., Maggi P., Haberl F., 2015a, A&A, 573, A73
Kavanagh P. J., Sasaki M., Whelan E. T., Maggi P., Haberl F., Bozzetto L. M., Filipović M. D., Crawford E. J., 2015b, A&A, 579, A63
Kavanagh P. J., Sasaki M., Bozzetto L. M., Points S. D., Filipović M. D., Maggi P., Haberl F., Crawford E. J., 2015c, A&A, 583, A121
Kavanagh P. J., et al., 2016, A&A, 586, A4
Kim S., Staveley-Smith L., Dopita M. A., Freeman K. C., Sault R. J., Kesteven M. J., McConnell D., 1998, ApJ, 503, 674
Kim S., Staveley-Smith L., Dopita M. A., Sault R. J., Freeman K. C., Lee Y., Chu Y.-H., 2003, ApJS, 148, 473
Lakićević M., et al., 2015, ApJ, 799, 50
Lasker B. M., 1977, ApJ, 212, 390
Leahy D. A., 2017, ApJ, 837, 36
Leahy D., Wang Y., Lawton B., Ranasinghe S., Filipović M., 2019, AJ, 158, 149
Lee J. H., Lee M. G., 2014, The Astrophysical Journal, 793, 134
Lin C. D.-J., Chu Y.-H., Ou P.-S., Li C.-J., 2020, The Astrophysical Journal, 900, 149
Long K. S., Dodorico S., Charles P. A., Dopita M. A., 1981, ApJ, 246, L61
Long K. S., Blair W. P., Kirshner R. P., Winkler P. F., 1990, ApJS, 72, 61
Long K. S., et al., 2010, ApJS, 187, 495
Long K. S., Blair W. P., Milisavljevic D., Raymond J. C., Winkler P. F., 2018, ApJ, 855, 140
Lopez L. A., Fesen R. A., 2018, Space Sci. Rev., 214, 44
Lopez L. A., Ramirez-Ruiz E., Huppenkothen D., Badenes C., Pooley D. A., 2011, ApJ, 732, 114
Mackey D., Koposov S., Da Costa G., Belokurov V., Erkal D., Kuzma P., 2018, ApJ, 858, L21
Maggi P., et al., 2014, A&A, 561, A76
Maggi P., et al., 2016, A&A, 585, A162
Maggi P., et al., 2019, A&A, 631, A127
Maitra C., et al., 2019, MNRAS, 490, 5494
Mathewson D. S., Clarke J. N., 1973, ApJ, 180, 725
Mathewson D. S., Healey J. R., 1964, Symposium - International Astronomical Union, 20, 245
Matonick D. M., Fesen R. A., 1997, The Astrophysical Journal Supplement Series, 112, 49
Matonick D. M., Fesen R. A., Blair W. P., Long K. S., 1997, ApJS, 113, 333
Maxted N. I., et al., 2018, ApJ, 866, 76
Millar W. C., White G. L., Filipovic M. D., 2012, Serbian Astronomical Journal, 184, 19
Neugent K. F., Massey P., Morrell N., 2018, ApJ, 863, 181
Oey M. S., 1996, ApJ, 465, 231
Oey M. S., Groves B., Staveley-Smith L., Smith R. C., 2002, AJ, 123, 255
Pennock C. M., van Loon J. T., Bell C., Filipović M., Joseph T., Vardoulaki E., 2020, arXiv e-prints, p. arXiv:2004.04531
Points S. D., Long K. S., Winkler P. F., Blair W. P., 2019, ApJ, 887, 66
Reid W. A., Parker Q. A., 2010, MNRAS, 405, 1349
Reid W. A., Stupar M., Bozzetto L. M., Parker Q. A., Filipović M. D., 2015, MNRAS, 454, 991
Russell S. C., Dopita M. A., 1990, ApJS, 74, 93
Sabbadin F., Minello S., Bianchini A., 1977, A&A, 60, 147
Sano H., et al., 2018, ApJ, 867, 7
Sano H., et al., 2019a, ApJ, 873, 40
Sano H., et al., 2019b, ApJ, 881, 85
Sano H., et al., 2020, arXiv e-prints, p. arXiv:2007.07900
Sasaki M., 2020, Astronomische Nachrichten, 341, 156
Sasaki M., et al., 2018, A&A, 620, A28
Schaerer D., Meynet G., Maeder A., Schaller G., 1993, A&AS, 98, 523
Seitenzahl I. R., Vogt F. P. A., Terry J. P., Ghavamian P., Dopita M. A., Ruiter A. J., Sukhbold T., 2018, ApJ, 853, L32
Seitenzahl I. R., Ghavamian P., Laming J. M., Vogt F. P. A., 2019, Phys. Rev. Lett., 123, 041101
Skrutskie M. F., et al., 2006, AJ, 131, 1163
Smith R. C., MCELS Team 1999, in Chu Y. H., Suntzeff N., Hesser J., Bohlender D., eds, IAU Symposium Vol. 190, New Views of the Magellanic Clouds. p. 28
Smith R. C., Kirshner R. P., Blair W. P., Winkler P. F., 1991, ApJ, 375, 652
Smith R. C., Kirshner R. P., Blair W. P., Long K. S., Winkler P. F., 1993, ApJ, 407, 564
Strüder L., et al., 2001, A&A, 365, L18
Stupar M., Filipović M. D., Jones P. A., Parker Q. A., 2005, Advances in Space Research, 35, 1047
Stupar M., Parker Q. A., Filipović M. D., 2008, MNRAS, 390, 1037
Stupar M., Parker Q. A., Frew D. J., 2018, MNRAS, 479, 4432
Sturm R., et al., 2013, A&A, 558, A3
Subramanian S., Subramaniam A., 2010, A&A, 520, A24
Turner M. J. L., et al., 2001, A&A, 365, L27
Vogt F., Dopita M. A., 2011, Ap&SS, 331, 521
Vogt F. P. A., Bartlett E. S., Seitenzahl I. R., Dopita M. A., Ghavamian P., Ruiter A. J., Terry J. P., 2018, Nature Astronomy, 2, 465
Vučetić M. M., Trčka A., Arbutina B., Ćiprijanović A., Pavlović M. Z., Urošević D., Petrov N., 2018, Astronomical and Astrophysical Transactions, 30, 379
Vučetić M. M., Onić D., Petrov N., Ćiprijanović A., Pavlović M. Z., 2019a, Serbian Astronomical Journal, 198, 13
Vučetić M. M., et al., 2019b, A&A, 628, A87
Warth G., Sasaki M., Kavanagh P. J., Filipović M. D., Points S. D., Bozzetto L. M., 2014, A&A, 567, A136
Westerlund B. E., Mathewson D. S., 1966, MNRAS, 131, 371
Williams B. J., Temim T., 2017, in Handbook of Supernovae, Alsabti A., Murdin P. (eds), Springer, Cham. pp 2105–2124, doi:10.1007/978-3-319-21846-5_94
Zaritsky D., Harris J., Thompson I. B., Grebel E. K., 2004, AJ, 128, 1606

de Horta A. Y., et al., 2012, A&A, 540, A25
di Benedetto G. P., 2008, MNRAS, 390, 1762

APPENDIX A: NOTES ON INDIVIDUAL OBJECTS

Below, we present notes on each individual source from this sample. These notes also include the number of OB stars found in the vicinity of each. As explained in Section 2.4, the significance of the number of OB stars is related to the possible classification of a SNR as a likely CC or a type Ia origin. This, together with the global (galactic) and local morphological properties, can indicate the potential of each of these individual objects to have a SN origin (Lopez et al. 2011) .

A1 J0444–6758 (Figure A1)

This object's Hα image shows patchy semi-circular diffuse emission with D=23.6 pc assuming the distance to the LMC of 50 kpc. This remnant candidate, as can be seen in Figure A1, is faint and it has a [S II]/Hα ratio of ~0.67 indicating it to be likely an SNR candidate. We searched the MCPS for the massive (OB) stars in and around this object's 100 pc boundaries and found that only one such star can be found at the far North position from the SNR candidate.

A bit of a caution for the classification of this object as an SNR candidate since [O III] lines are quite prominent while at the same time we note an absence of the [O I] line. The MCELS [O III] image also shows emission concentrated in the centre rather than in a shell. Unfortunately, this area is presently poorly covered in X-ray surveys and further study is needed.

A2 J0450–6818 (Figure A2)

The Hα image for this object shows two distinctly disjointed filaments, giving a bilateral and elliptical shell morphology. The emission lines are strongest in these areas. The [S II]/Hα ratio is ~0.8 and has an elliptical diameter of about 116×87 pc which satisfies one of the selection criteria for the larger diameter class of SNRs known as "evolved" (Mathewson & Clarke 1973). This remnant, as seen in Figure A2, was also detected in [O I] which boosts the SNR confirmation as it gives evidence of shock heating. As for the J0444–6758 SNR candidate, the stellar content of this object's area shows the presence of only one nearby massive OB star.

A3 J0454–7003 (Figure A3)

This circular object is positioned at the outer south-east boundary of the large superbubble DEM L25 (Oey et al. 2002). With a diameter of 30 pc (Figure A3) and no optical spectra available for this object, we use MCELS images and estimate that the overall [S II]/Hα ratio of >0.8 which warrants further investigation of this object as an SNR candidate. For the larger DEM L25 shell, the [O III]/Hα ratio is also higher in the interaction zone (ranging around 0.8), which together with the high [S II]/Hα ratio suggest a ram pressure-induced shock. We note that there is also a possible filamentary shell ("blow-out") from the much larger and brighter DEM L25 shell. There are a number of nearby OB stars in projection to J0454–7003, and their stellar content was classified by Oey (1996).

Very weak and soft (<0.7 keV) X-ray emission is seen around the centre of the ellipse marking the optical emission (Figure A3 (right)). Clearly extended soft X-ray emission is detected from the nearby DEM L25 shell. Unfortunately, the exposure of ~3.8 ks (EPIC-pn) is too short for a more quantitative analysis of the X-ray emission from J0454–7003.

A4 J0455–6830 (Figure A4)

The MCELS Hα image of this SNR candidate does not show an obvious shell morphology with diffuse and scattered emission across the suggested boundaries (Figure A4). This SNR candidate has the smallest diameter (D_{av}=17 pc) of our sample and the [S II]/Hα ratio of ~1.1 is one of the sample's highest.

As in J0450–6818, this SNR candidate also exhibits prominent (bright) [O III] lines while at the same time we did not detect an [O I] line. The MCELS [O III] image also shows distinctive emission that, in this case, follows the Hα and [S II] emission. Finally, one would expect that such a small sized SNR would be bright in X-ray emission. Unfortunately, this area is presently poorly covered in all X-ray surveys.

We also searched MCPS for massive (OB) stars near this object (100 pc radius) and found 18 very distant OB stars – none within the boundaries of this proposed SNR candidate.

A5 J0500–6512 (Figure A5)

The Hα image shows a looped filamentary structure (Figure A5). This SNR candidate has a complex (double-shell) morphology, with the shells overlapping in the South. We estimate that this is similar in size to the J0450–6818 candidate. The [S II]/Hα ratio is ~0.81, typical of SNRs. The limited variety of line intensities are not surprising as the weaker lines are lost in the noise.

A6 J0502–6739 (Figure A6)

This SNR candidate structure has an average diameter of 43 pc and shows diffuse structureless emission which is slightly elongated (Figure A6). Although the [S II]/Hα ratio is relatively low at ~0.55, we still take this as an SNR candidate but we note possible contamination from the nearby H II region.

As for other objects in this sample, we searched for massive stars and found the richest population of OB stars (18 with 2 inside the object boundaries) among the sample studied here.

A7 J0506–6509 (Figure A7)

The candidacy for the SNR nature of this object is prompted by its spherical (circular) shell morphology with a diameter of 90 pc (Figure A7). While there are no spectra available for this candidate, we use MCELS images and estimate that the overall [S II]/Hα ratio is ~0.6, which warrants further investigation of this object as an SNR candidate. We note that no nearby massive stars could be found.

A8 J0508–6928 (Figure A8)

This SNR candidate has an obvious half-shell (horse-shoe) morphology in the top-half, expanding a little past half-way (Figure A8). The [S II]/Hα ratio is ~0.72. This remnant also has the highest peak in Hα in our sample but given the strength of Hβ in this object, we note the stunning lack of any [O III] emission. We find 2 massive OB stars inside the object bounds, 3 just north and 2 relatively close on the Eastern side of this SNR candidate.

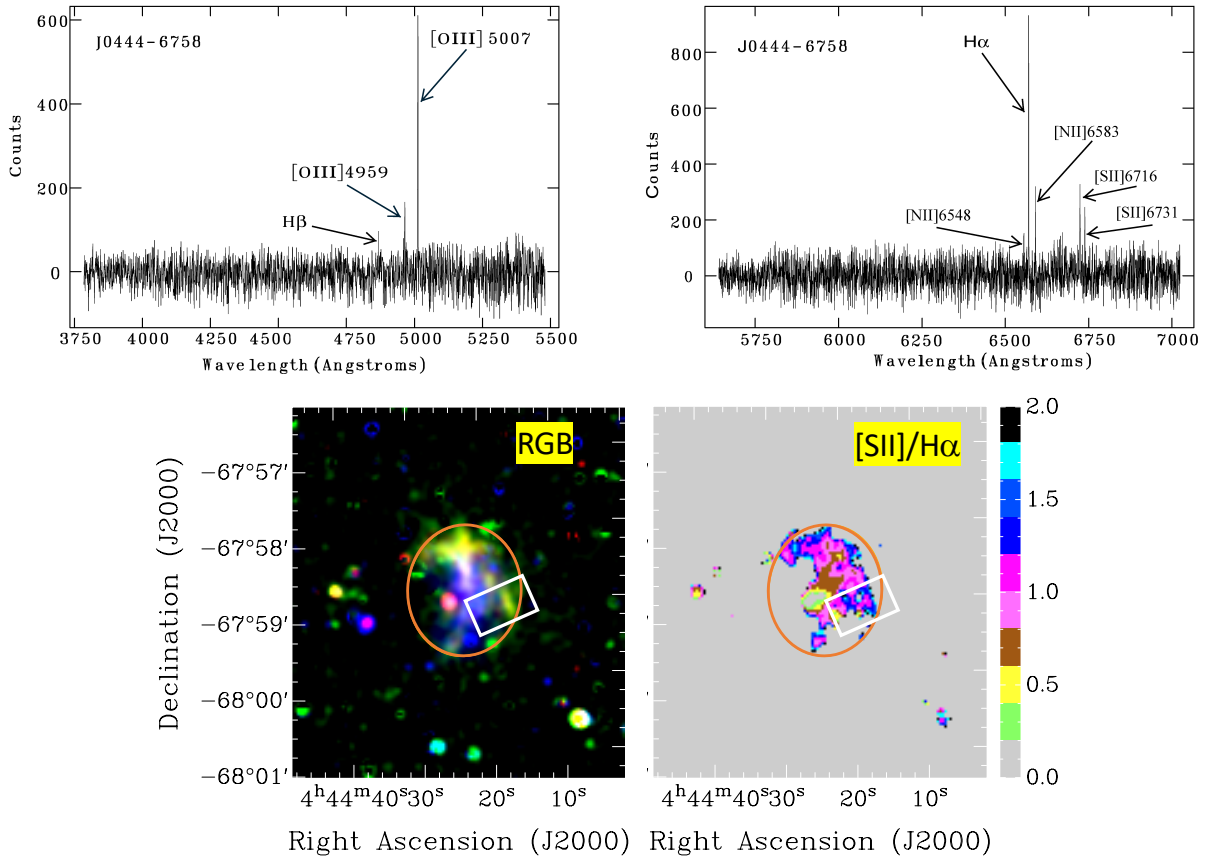

Figure A1. J0444–6758: (Top) showing the spectra from both arms (left; blue, right; red) of the spectrograph; (Bottom) colour images produced from MCELS data, where RGB corresponds to Hα, [S II] and [O III] while the ratio map is between [S II] and Hα. The rectangular box (white) represents an approximate position of the WiFeS slicer. The orange ellipse indicates the extent of the optical emission seen from the object.

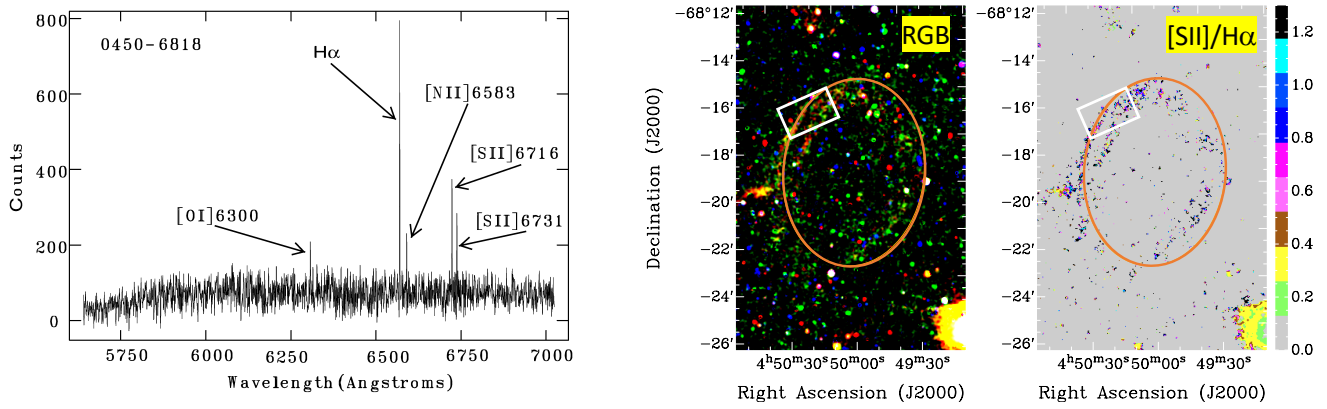

Figure A2. J0450–6818: (Left) showing the spectra from one arm (red) of the spectrograph; (Middle and right) colour images produced from MCELS data, where RGB corresponds to Hα, [S II] and [O III] while the ratio map is between [S II] and Hα. The rectangular box (white) represents an approximate position of the WiFeS slicer. The orange ellipse indicates the extent of the optical emission seen from the object.

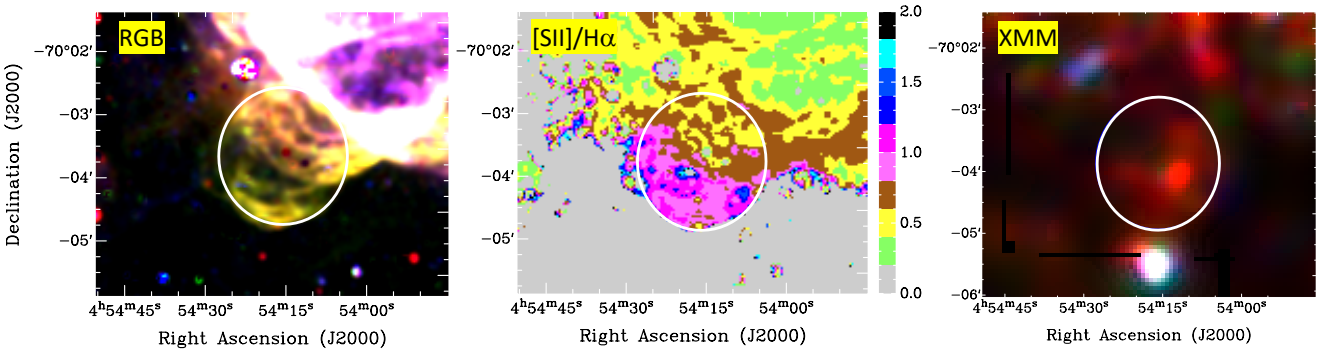

Figure A3. J0454–7003: colour images produced from MCELS data, where RGB corresponds to Hα, [S II] and [O III] (left) while the ratio map is between [S II] and Hα (middle). *XMM-Newton* EPIC RGB (R=0.3–0.7 keV band, G=0.7–1.1 keV band and B=1.1–4.2 keV band) image from the area of J0454–7003 is shown in the right panel. The white circle indicates the extent of the optical emission seen from the object. The line-shaped features in the left and bottom hand side of the image are smoothing artefacts, caused by borders of adjacent observations, which introduce steps in exposure.

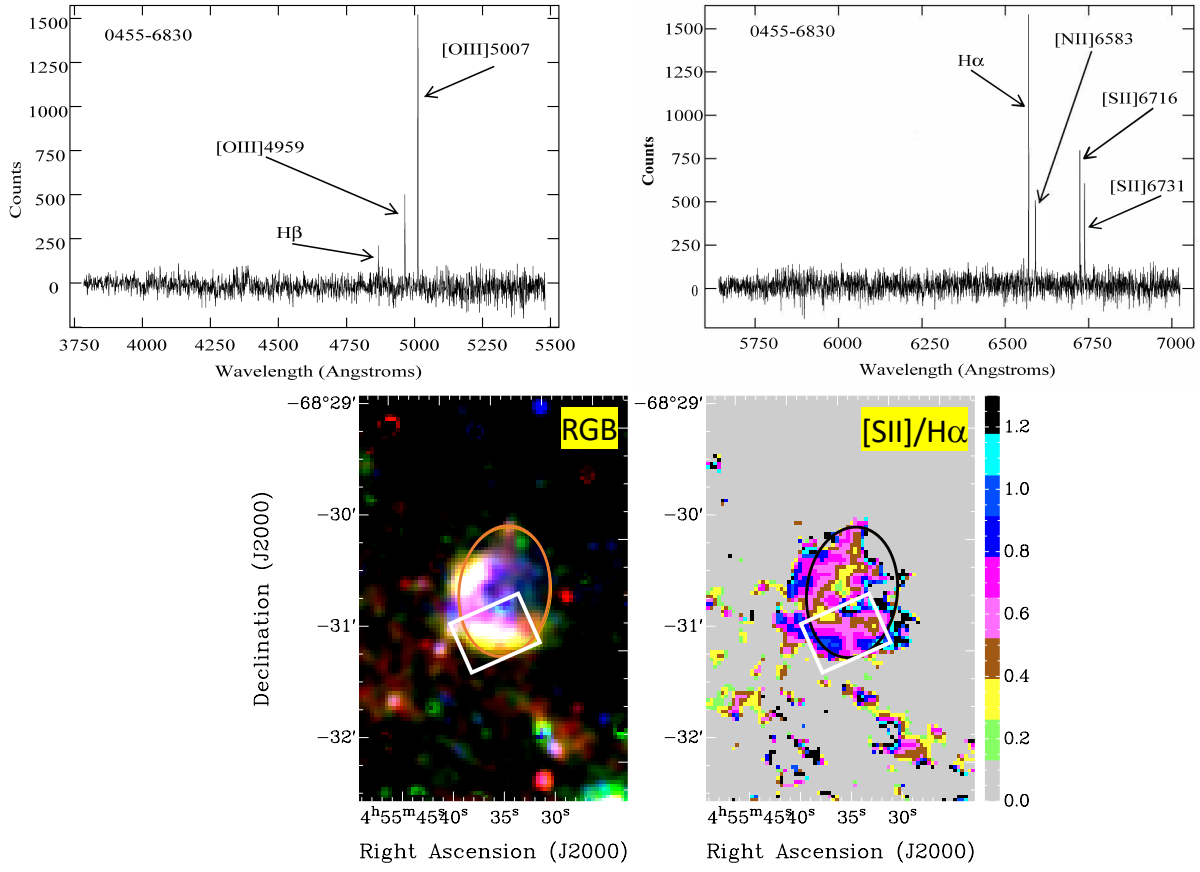

Figure A4. J0455–6830: (Top) showing the spectra from both arms (left; blue, right; red) of the spectrograph; (Bottom) colour images produced from MCELS data, where RGB corresponds to Hα, [S II] and [O III] while the ratio map is between [S II] and Hα. The rectangular box (white) represents an approximate position of the WiFeS slicer. The orange/black ellipse indicates the extent of the optical emission seen from the object.

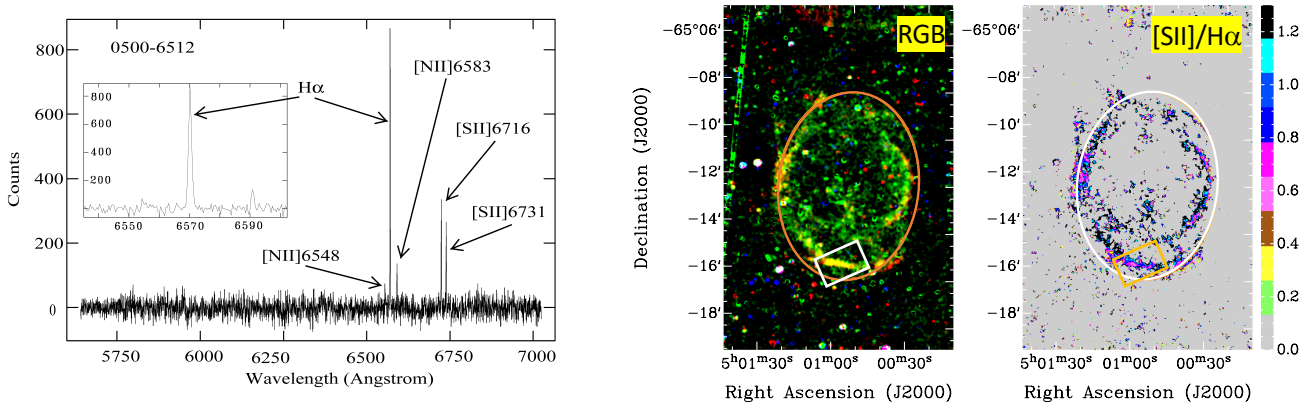

Figure A5. J0500–6512: (Left) showing the spectra from one arm (red) of the spectrograph where the inset figure represents the "zoomed-in" Hα line. This Hα line is detected with the broadening of 1.20 Å while the instrument width is ~1 Å (~45 km s^{-1}); (Middle and right) colour images produced from MCELS data, where RGB corresponds to Hα, [S II] and [O III] while the ratio map is between [S II] and Hα. The rectangular box (white/orange) represents an approximate position of the WiFeS slicer. The orange/white ellipse indicates the extent of the optical emission seen from the object.

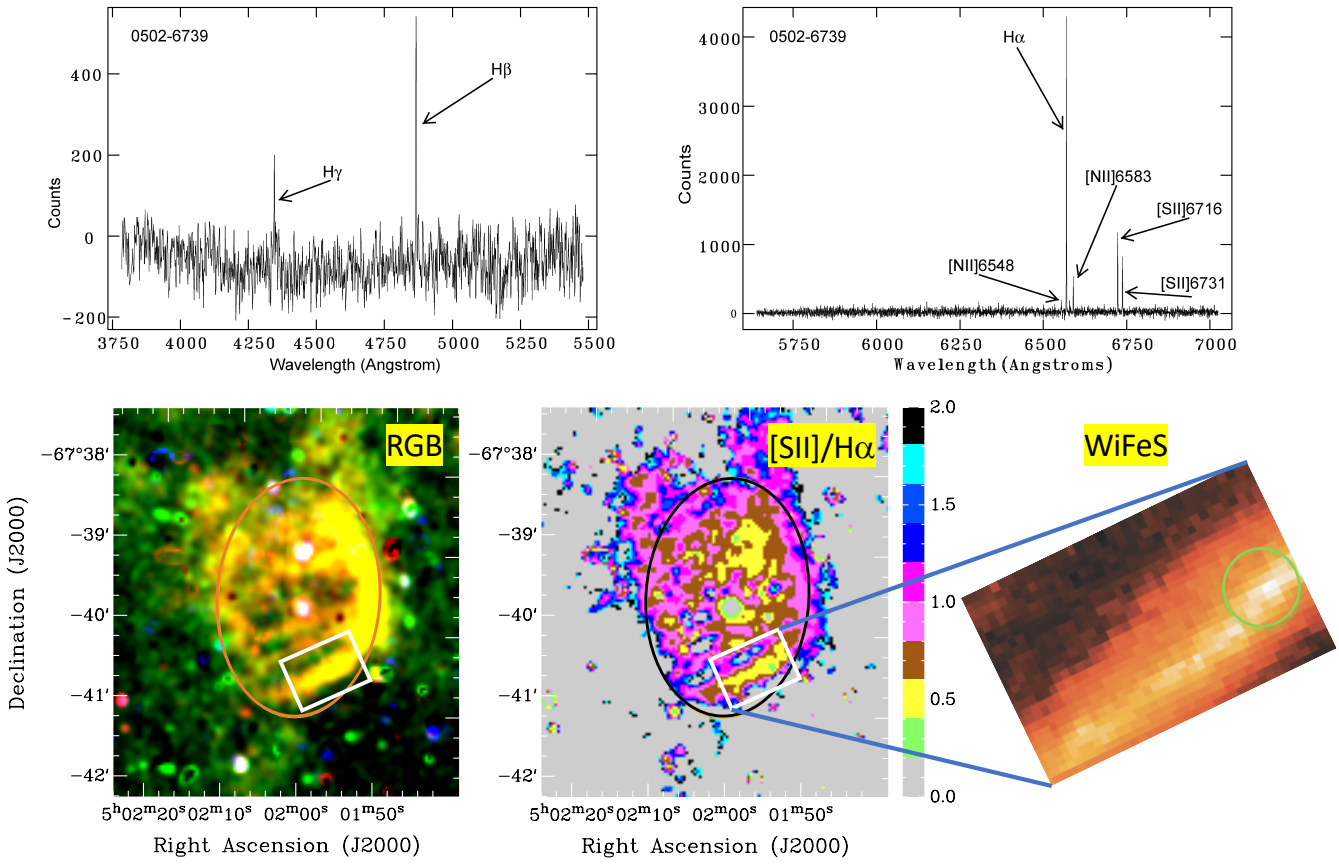

Figure A6. J0502–6739: (Top) showing the spectra from both arms (left; blue, right; red) of the spectrograph; (Bottom left and right) colour images produced from MCELS data, where RGB corresponds to Hα, [S II] and [O III] while the ratio map is between [S II] and Hα. The orange/black ellipse indicates the extent of the optical emission seen from the object. (bottom right) image of 25×38 arcsec (as in the white rectangular box) field of view of WiFeS spectrograph slicer which consists of 3152 slices (see Sect. 2.2). The strongest part of Hα emission of J0502–6739 is detected on slice number 2116. The green circle represents the position of the highest flux within a 10 arcsec aperture where the 1D spectrum of all spectral lines is extracted from the cube.

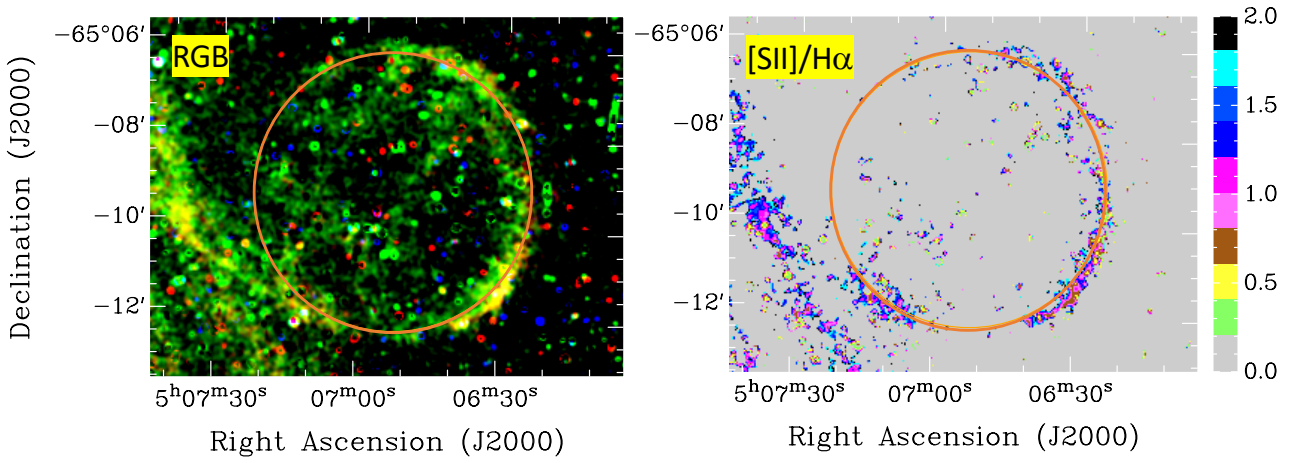

Figure A7. J0506–6509: colour images produced from MCELS data, where RGB corresponds to Hα, [S II] and [O III] while the ratio map is between [S II] and Hα. The orange circle indicates the extent of the optical emission seen from the object.

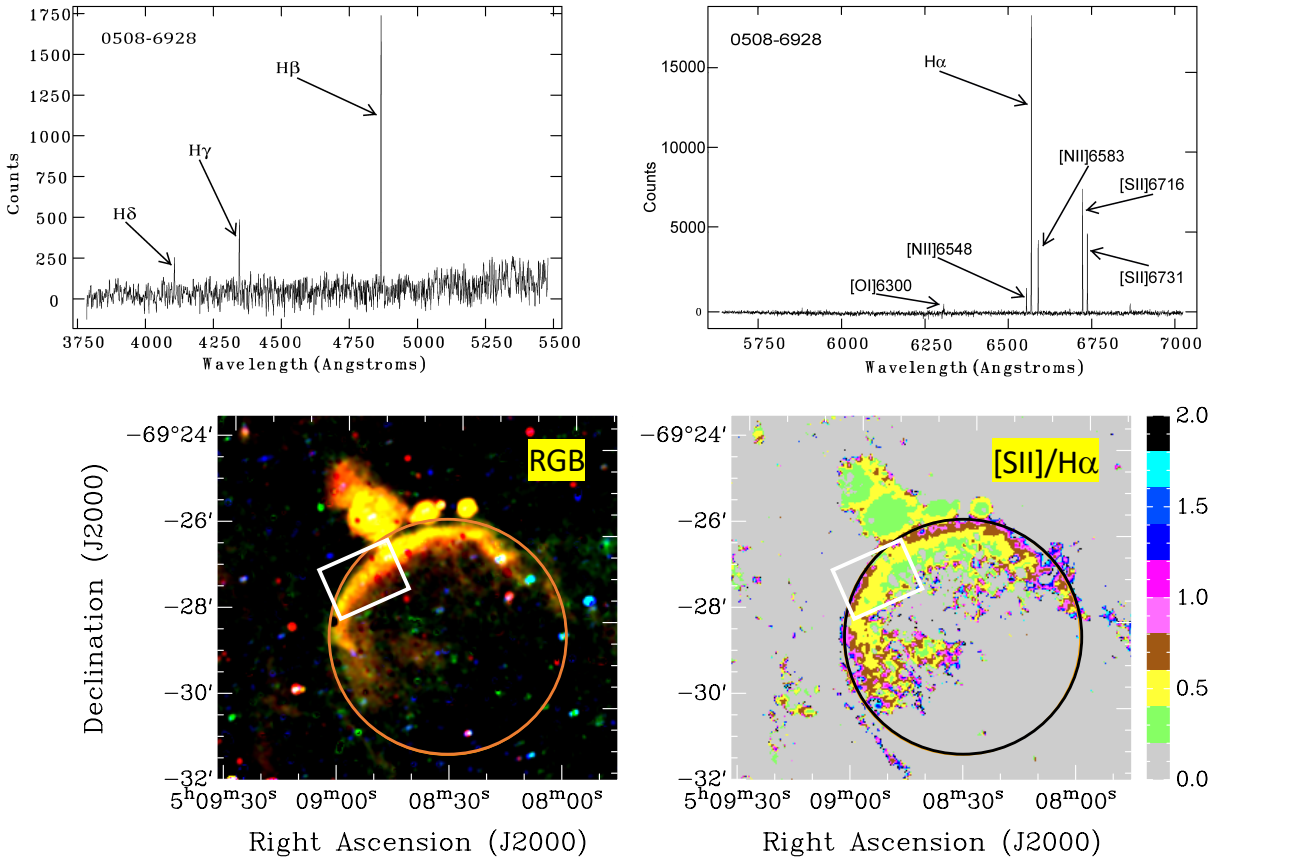

Figure A8. J0508–6928: (Top) showing the spectra from both arms (left; blue, right; red) of the spectrograph; (Bottom) colour images produced from MCELS data, where RGB corresponds to Hα, [S II] and [O III] while the ratio map is between [S II] and Hα. The rectangular box (white) represents an approximate position of the WiFeS slicer. The orange/black circle indicates the extent of the optical emission seen from the object.

A9 J0509–6402 (Figures A9 and A10)

This SNR candidate lies 2° north of the LMC main body, in a field where we did not expect detection of any LMC SNRs. The MCELS Hα and [S II] images shows a typical (shell-like) SNR morphology but somewhat elongated (Figure A9). At the same time, we report no [O III] emission in the MCELS image. Due to the size of the J0509–6402 shell ~8′ × 5′ (~116×83 pc), the SNR candidate cannot be morphologically classified as a young SNR. If confirmed as an SNR, this object would be certainly evolving in a much more rarefied environment than the rest of the known LMC SNRs. However, as can be seen in Figure A10, the eastern side of J0509–6402 might be interacting with one the northernmost H I spurs and perhaps create so called cloud-cloud interaction as seen in a number of other MCs SNRs and shells (Sano et al. 2018, 2019a,b, 2020). Sensitive X-ray and molecular gas observations are needed to confirm this possibility.

The optical spectra confirms shocks typical of SNRs which can be further confirmed using the ratio of shock sensitive [S II] lines with Hα e.g. [S II]/Hα ratio of 0.75 (see Table 2) which differentiates SNRs from H II regions and planetary nebulae. The most prominent line in its spectrum is Hα, with the presence of [O I] at 6300Å, [N II] at 6548Å and 6583Å as well as [S II] lines at 6717Å and 6731Å. All these lines are always associated with spectra of SNRs except the [O I] line which is rarely seen. We estimate that this SNR has an electron density of ~30 cm^{-3} (for a temperature of 10 000 K) as a result of the ratio of [S II] lines. This indicates that SNR candidate J0509–6402 is most likely of a mature age. We also suggest that it might be more likely a result of a type Ia SN event because of its large distance from the main body of the LMC where massive stars are rarely found. However, one cannot completely disregard a possible core-collapse SN event as a very massive star could be ejected from the LMC main body and survive "traveling" some ~2 kpc (assuming a distance to the LMC of 50 kpc). While no such SN explosion is directly confirmed (so far) we suggest that only a small fraction of such SNRs would exist in any galaxy. In principle, this scenario could be applied to any CC type of SN explosion unless a given SNR doesn't currently sit near a known OB star.

As this object is so far north of the main body of the LMC we could not search for massive stars since the area is not covered in Zaritsky et al. (2004).

A10 J0517–6757 (Figure A11)

The MCELS Hα image (Figure A11) of this SNR candidate shows a faint, thin half-shell of emission towards the south of the object. It also shows line intensities for Hγ and Hβ in its spectrum. J0517–6757 is surrounded with a number of H II regions, the most prominent of which is located just north of its suggested boundaries. Although unconfirmed, given that its [S II]/Hα ratio is ~0.69 and a somewhat typical LMC SNR size of D=39 pc, we nominate this object to be an SNR candidate. While we find some 17 OB stars in a 100 pc radius, none of these lie within the object's defined shell.

We also note an adjacent semi-loop somewhat north of our SNR candidate J0517–6757 (see dashed ellipse in Figure A11). With an elevated [S II]/Hα ratio of 0.6 and diameter of ~150 arcsec (~36 pc), it will be further studied in our future follow up studies.

A11 MCSNR J0522–6740 (Figure A12)

This source shows a diffuse elliptical shell morphology (D=87×65 pc) which is indicative of an evolved SNR (Figure A12 (left and middle)). It is found just outside the northern boundary of the giant H II complex LHA 120-N 44 (Henize 1956). While there are no optical spectra available for this object, the source is most prominent in the light of [S II], and we estimate from the MCELS images a very high [S II]/Hα ratio of ~1.0. There are several isolated filaments where the [S II]/Hα ratio is elevated (>0.4). But, we couldn't connect any of these with possible new SNR candidates. Seven massive OB stars are found in the vicinity, but only one within the bounds of this SNR candidate.

Although the contour plot is located in a region with low X-ray exposure (~10 ks EPIC-pn combining two observations), soft extended X-ray emission is significantly detected at the centre of the optical shell (Figure A12, right), most prominently in the 0.7–1.1 keV band. We analysed the X-ray spectrum of MCSNR J0522–6740 accumulated over the whole optical shell. The spectrum is thermal and reproduced by the emission of an optically-thin collisional-ionisation equilibrium plasma at LMC abundance (about half-solar). The best-fit electronic temperature is $kT_e = 0.3 \pm 0.02$ keV. This is typical for evolved SNRs, lending strong support to its confirmation as a bona-fide SNR. The amount of LMC neutral gas in front of the source is low (best-fit $N_H = 0$, and less than 10^{21} cm^{-2} at the 90 % confidence level), but the total LMC line-of-sight integrated H I column at this position is only 1.6×10^{21} cm^{-2} (Kim et al. 2003). The 0.3–8 keV luminosity of MCSNR J0522–6740 is $L_X = 1.7 \times 10^{34}$ erg s^{-1}, potentially ranking this source among the 10 per cent faintest (so far) LMC SNRs in X-rays.

We investigate whether the prominence of the medium 0.7–1.1 keV X-ray band could be due to the presence of elevated iron abundance of SN ejecta origin, as was seen previously in several LMC and SMC SNRs (e.g. Borkowski et al. 2006; Maggi et al. 2014; Kavanagh et al. 2016; Maggi et al. 2019). When letting the oxygen and iron abundance free, fits with elevated Fe abundance are favoured despite large uncertainties (the upper value of Fe abundance is unconstrained), but the statistical improvement is moderate ($\Delta\chi^2 = 4.95$ for 2 degrees of freedom, i.e. less than 2σ). Exploring the parameter space of oxygen vs. iron abundance, the Fe/O ratio (by number) is > 3 at the 90 % confidence level. This is more than twice the average LMC value of 1.4. We consider this enhancement to be indicative of a possible detection of iron ejecta. However, this evidence remains marginal given the limited exposure time and spectral resolution, and the intrinsic faintness of MCSNR J0522–6740.

Based on above findings, we suggest that MCSNR J0522–6740 is a new LMC SNR.

A12 J0528–7017 (Figure A13)

The SNR nature of J0528–7017 is drawn from its spherical (circular) shell morphology with a diameter (D=81 pc; Figure A13) while MCELS images indicates an overall [S II]/Hα ratio of ~0.9. We searched MCPS images for massive (OB) stars near this object within a 100 pc radius and found 13 very distant OB stars from which 4 are within the boundaries of this proposed SNR candidate.

A13 J0529–7004 (Figure A14)

The candidacy for the SNR nature of J0529–7004 is also suggested by its spherical (circular) shell morphology with a diameter of 47 pc (Figure A14). While there are no spectra available for this candidate, we use MCELS images and found that the overall [S II]/Hα ratio of ~1.0 warrants further investigation of this object as an SNR candidate. We note that no massive stars could be found within the

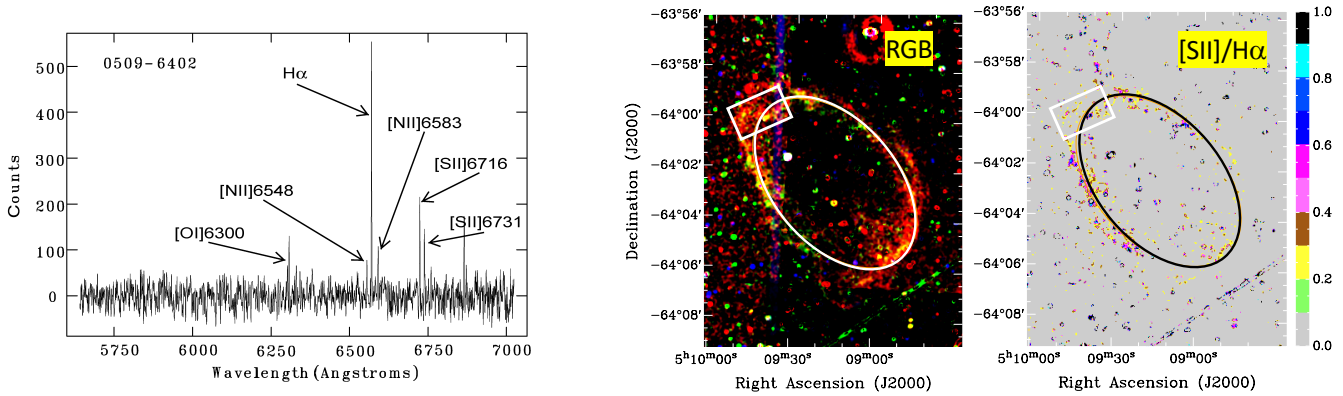

Figure A9. J0509–6402: (Left) showing the spectra from one arm (red) of the spectrograph; (Middle and right) colour images produced from MCELS data, where RGB corresponds to Hα, [S II] and [O III] while the ratio map is between [S II] and Hα. The rectangular box (white) represents an approximate position of the WiFeS slicer. The white/orange ellipse indicates the extent of the optical emission seen from the object.

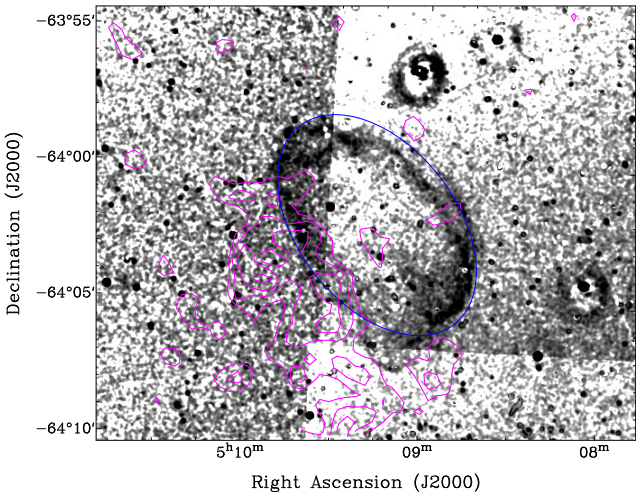

Figure A10. Hα image of J0509–6402 overploted with H I contours (6, 7, 8 and 9×10^{20} atoms cm^{-2}. The blue ellipse indicates the extent of the optical emission seen from the object.

shell of this object but in a near vicinity (100 pc radius) we found 12 OB stars in the MCPS.

J0529-7004 is covered by two XMM-Newton observations, but both are at the very edge of the EPIC field of view. This results in an uneven exposure with 7.5 ks in the eastern and 25 ks in the western half of the region with optical emission. This candidate is located in an area of strong diffuse emission, but peaked soft X-ray emission is detected from J0529–7004 right at the centre of the optical emission. The position of the *ROSAT* source [HP99] 1077 is consistent with the bright spot seen in the EPIC image. The position of the *ROSAT* X-ray source source [HP99] 1077, which is about 18.5″ away from the centre of J0529–7004, is consistent with the bright spot seen in the EPIC image.

A14 J0538–7004 (Figure A15)

This SNR candidate shows a partial filled-in shell, concentrating to the North-West (Figure A15). There are no spectra available for this candidate but the [S II]/Hα ratio of ∼0.8 that we estimate from the MCELS images is indicative of an SNR nature. However, this is the second smallest SNR candidate in our 19 object strong sample with D_{av}=19.4 pc. This would strongly argue for the presence of radio and X-ray emission which we don't see in any of our surveys despite the good coverage. Only two distant OB stars are found within the 100 pc from the object centre. As for the J0444–6758 (Section A1), we see a bright central [O III] emission which is indicative of an H II region. Therefore, this object is in a group of low confidence SNR candidates in this sample.

A15 MCSNR J0541–6659 (Figures A16 and A17)

This source was previously suggested as an SNR in the LMC based on its initial X-ray detection (Grondin et al. 2012). It was named [HP99] 456 in the *ROSAT* PSPC survey of the LMC (Haberl & Pietsch 1999, hereafter HP99). West of the X-ray source, there is an extended source in the optical bands. Here, for the first time, we present optical spectra of this object (see Figure A16). It has some diffuse emission towards the top left and relatively low [S II]/Hα ratio of ∼0.4. We note a large peak in Hα and Hβ which coupled with its [O III] value, gives a low [O III]/Hβ ratio. Therefore, this SNR is possibly located next to an H II region.

We obtained data from a 50 ks observation with the *Chandra* X-ray Observatory, using the ACIS-S array in VFAINT mode. The SNR was observed at the aimpoint and was fully covered by the S3 chip. The observation was split into two parts with the same configuration: one observation performed on June 18, 2015 (ObsID 17675) with a net exposure time of 22 ks and another one performed 9 days later on June 27, 2015 (ObsID 16754) with a net exposure time of 29 ks. We reprocessed the data using CIAO Version 4.7 and CALDB Version 4.6.7. Using the reprocessed files, we created images in two bands: soft band (0.3–1.0 keV) and hard band (1.0–8.0 keV). We then smoothed the images adaptively using the tool `dmimgadapt` with a Gaussian kernel. We also merged the event files of the two observations and created images.

The *Chandra* images show shell-like soft X-ray emission and confirm the SNR identified with *XMM-Newton* data (Figure A17). There is some additional faint soft diffuse emission extending to the northeast, which might be caused by acceleration of gas along a negative density gradient (possible "blow out"). One should also consider that the SNR has blown out as we can see open optical filaments in that direction in the MCELS images.

Above 1 keV, extended emission is only visible in the western

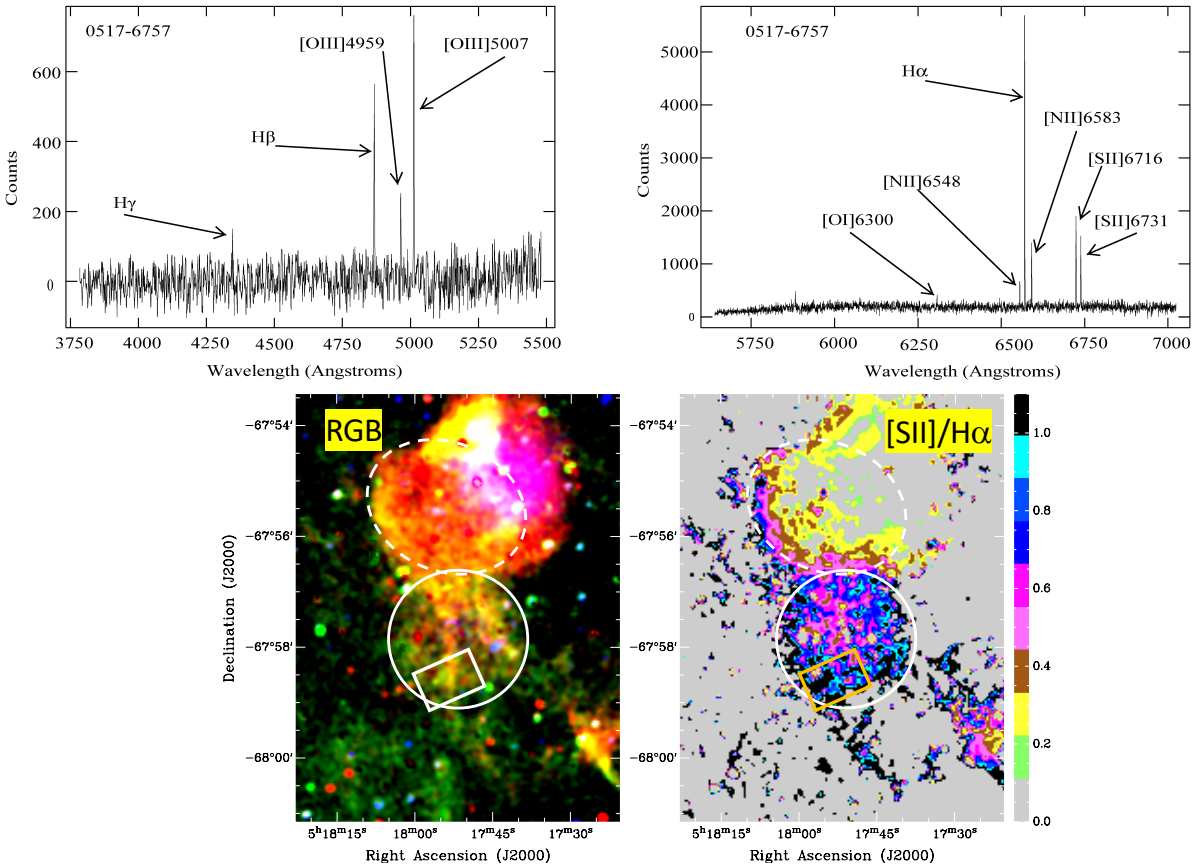

Figure A11. J0517–6757: (Top) showing the spectra from both arms (left: blue, right: red) of the spectrograph; (Bottom) colour images produced from MCELS data, where RGB corresponds to Hα, [S II] and [O III] while the ratio map is between [S II] and Hα. The rectangular box (white/orange) represents an approximate position of the WiFeS slicer. The solid white circle indicates the extent of the optical emission seen from the object while the dashed ellipse indicates possible adjacent SNR candidate that we will investigate in our future studies.

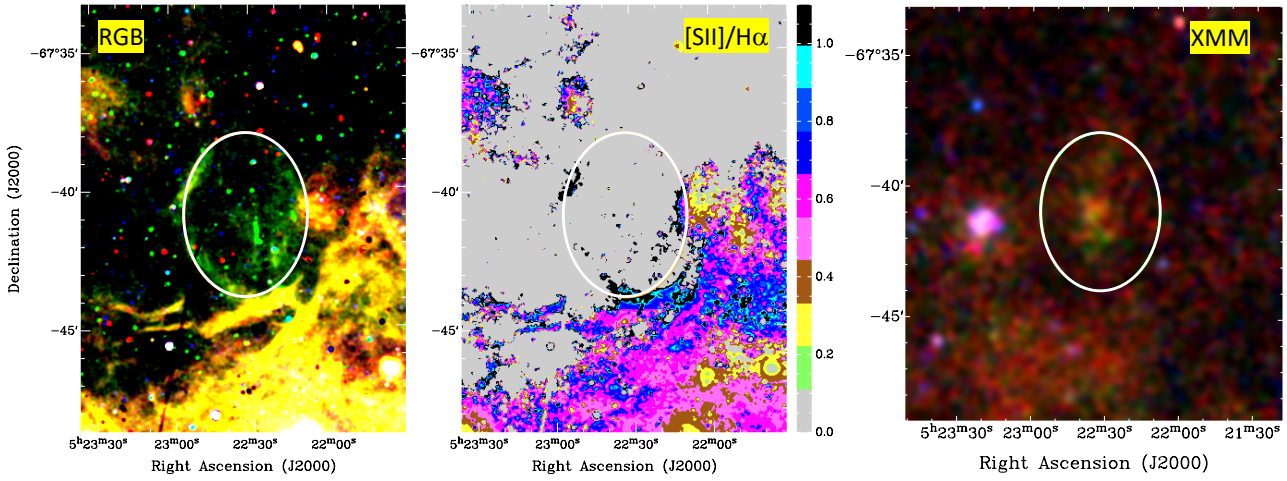

Figure A12. MCSNR J0522–6740: colour images produced from MCELS data, where RGB corresponds to Hα, [S II] and [O III] (left) while the ratio map is between [S II] and Hα (middle). *XMM-Newton* EPIC RGB (R=0.3–0.7 keV band, G=0.7–1.1 keV band and B=1.1–4.2 keV band) image from the area of MCSNR J0522–6740 is shown in the right panel. The white ellipse indicates the location of the optical shell.

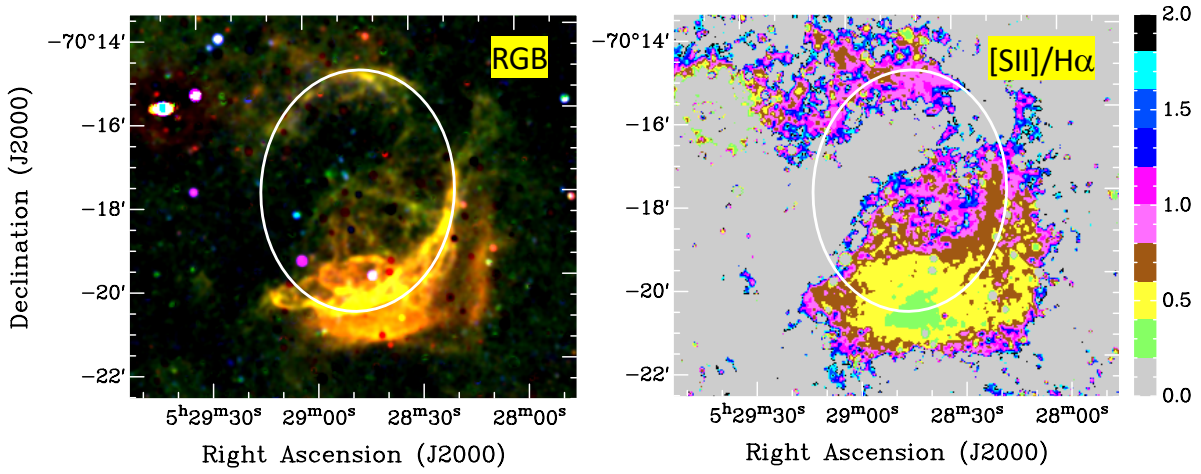

Figure A13. J0528–7017: Colour images produced from MCELS data, where RGB corresponds to Hα, [S II] and [O III] while the ratio map is between [S II] and Hα. The white ellipse indicates the location of the optical shell.

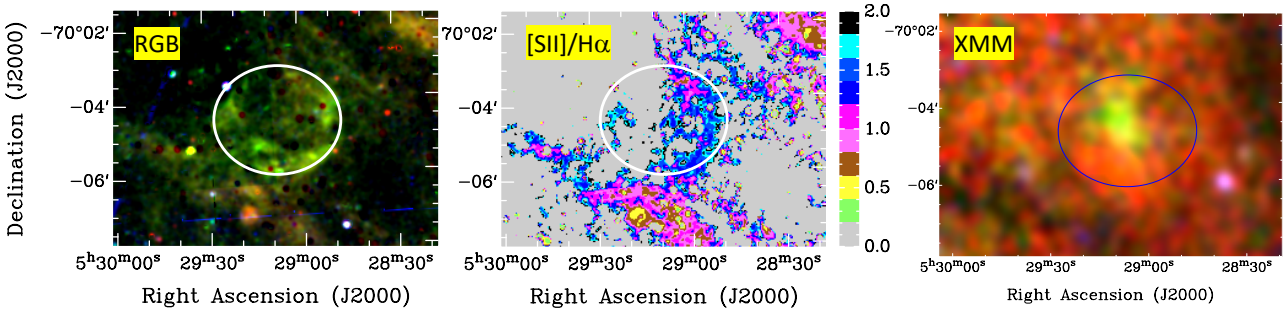

Figure A14. J0529–7004: colour images produced from MCELS data, where RGB corresponds to Hα, [S II] and [O III] (left) while the ratio map is between [S II] and Hα (middle). *XMM-Newton* EPIC RGB (R=0.3–0.7 keV band, G=0.7–1.1 keV band and B=1.1–4.2 keV band) image from the area of J0529–7004 (right). The white/blue ellipse indicates the location of the optical shell.

part, as had been already discovered with *XMM-Newton*. Inside the hard extended emission, which has an extent of ∼80″× 100″, the superb spatial resolution of *Chandra* allowed us to detect two point sources: CXOU J054138.2–665817 (PSN) and CXOU J054140.4–665912 (PSS). These sources were detected by applying the source detection procedure `wavdetect` on the images of the different bands for both observations. For PSN, we only obtained ∼ 20 net counts. The source is hard and only detected in the hard-band image. Source PSS has ∼ 60 net counts and is detected both in the soft and the hard-band images. However, there is no indication that one of these sources might be a pulsar. In fact, according to Maggi et al. (2016), the stellar population in the region around the SNR is rather old with an age of $> 5\times10^7$ years for the majority of the stars (based on the Magellanic Clouds Photometric Survey, MCPS, Zaritsky et al. 2004), which indicates that most of massive stars have ended their lives (Schaerer et al. 1993). In fact, a number of OB stars can be found within the 100 pc of the SNR centre from which only two are within its boundaries.

A16 MCSNR J0542–7104 (Figure A18)

This is a large, elliptical SNR candidate with a filled-in centre shell morphology (Figure A18) that extends to 73×51 pc. The [S II]/Hα ratio estimated from our spectroscopic observation is ∼0.82 which is typical of SNRs. As for a number of other objects from our sample, this SNR candidate does not show any detectable radio-continuum emission in our surveys. However, we note the detection of a source at this position in the *ROSAT* survey as HP[99] 1235. Further *XMM-Newton* follow up observations of this source will be presented in Kavanagh at al. (2020; in prep.) and we can consider this object as a bona-fide SNR. We also note that only one but very distant OB star is found at some 90 pc distance from the centre of this object.

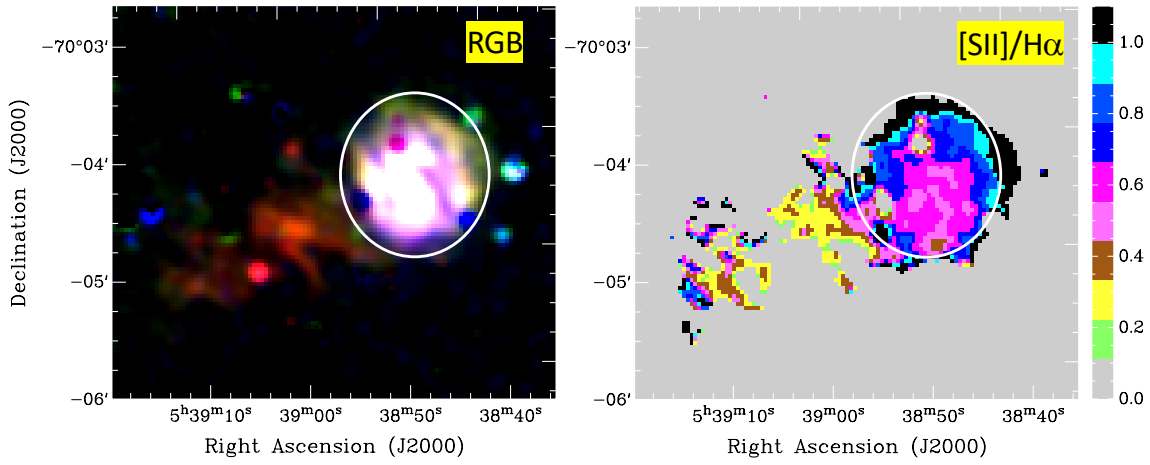

Figure A15. J0538–7004: colour images produced from MCELS data, where RGB corresponds to Hα, [S II] and [O III] while the ratio map is between [S II] and Hα. The white circle indicates the location of the optical shell.

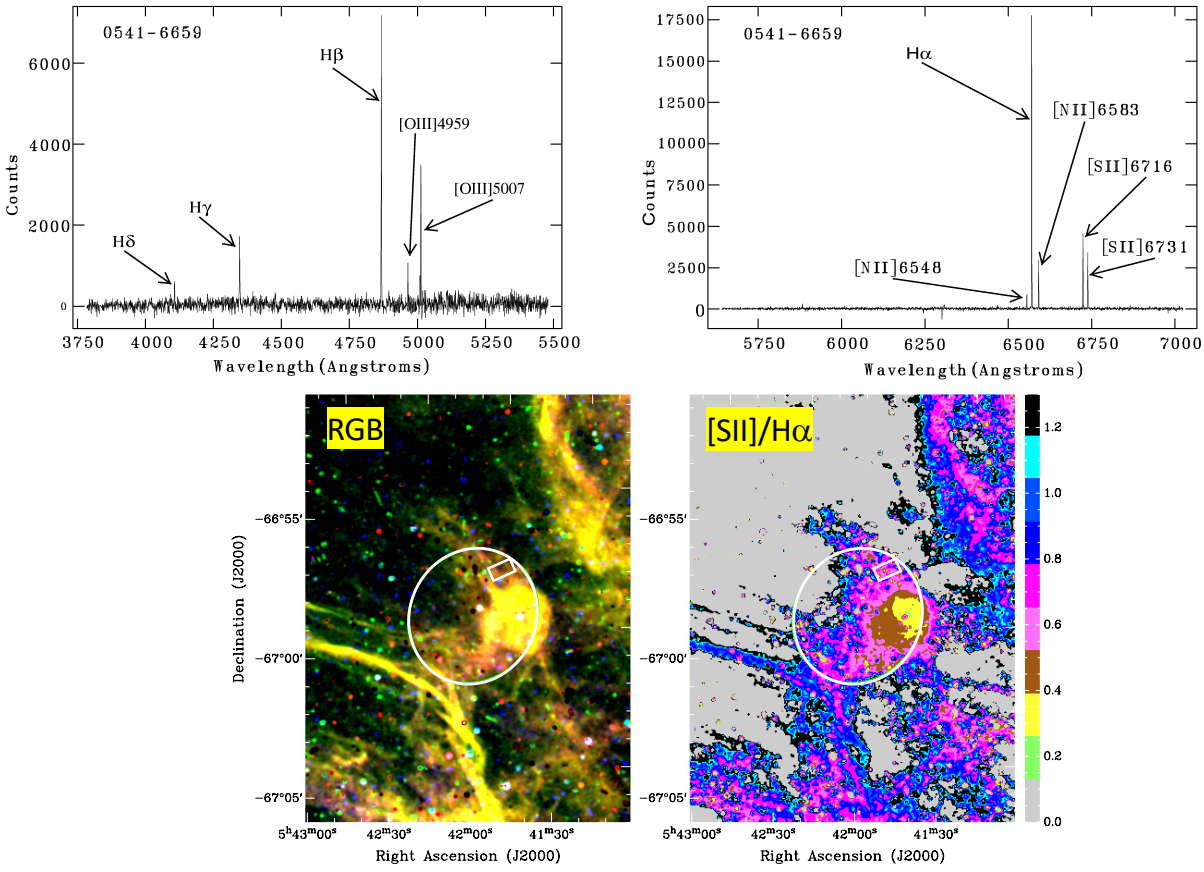

Figure A16. MCSNR J0541–6659: (Top) showing the spectra from both arms (left; blue, right; red) of the spectrograph; (Bottom) colour images produced from MCELS data, where RGB corresponds to Hα, [S II] and [O III] while the ratio map is between [S II] and Hα. The rectangular box (white) represents an approximate position of the WiFeS slicer. The white circle indicates the location of the optical shell.

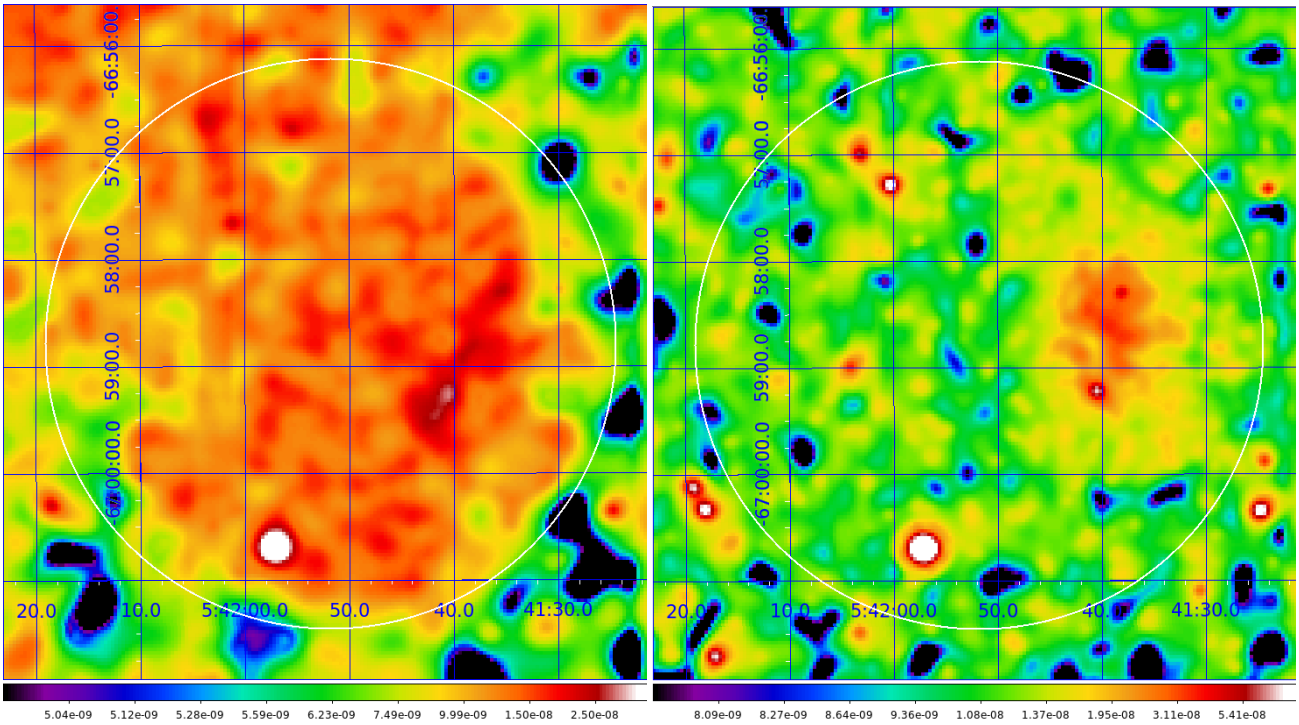

Figure A17. *Chandra* ACIS images of MCSNR J0541–6659 created from merged data of observations 16754 and 17675 (left: soft-band image, 0.3–1.0 keV; right: hard-band image, 1.0–8.0 keV). The images have been binned with a bin size of 4 pixels, smoothed adaptively, and exposure-corrected. The shell of the SNR is indicated with a white circle.

A17 J0548–6941 (Figure A19)

This candidate has an obvious half shell elongated morphology to its south-west (Figure A19) and a somewhat smaller size of 38×23 pc. It has a [S II]/Hα ratio of ~0.6 (from our WiFeS spectroscopic observations) and is the only SNR candidate in the sample with a [Fe II] line. We find 4 distant OB stars in the area of SNR candidate J0548–6941. This region is covered by *XMM-Newton* and reveals no X-ray emission.

A18 J0549–6618 (Figure A20)

J0549–6618 has no obvious shell morphology like many other objects in our sample but has a filled-in centre (Figure A20). There are no spectra available for this candidate but our [S II]/Hα ratio estimates based on the MCELS images is ~1.0. The stellar environment is such that we can't see any nearby massive star.

A19 J0549–6633 (Figure A21)

This SNR candidate is chosen based on its very high MCELS [S II]/Hα ratio of 1.4 (Figure A21; Table 2). While elongated (D=131×95 pc), it also has a centre-filled-in shell morphology but without a distinctive peak at the centre. It is the largest among all of the objects studied here and it has the highest spectroscopic [S II]/Hα ratio at ~1.38. The remnant is not only strong in [S II] but is also detected in [O I]. As shown in Figure 2, this source is just outside of the established spectroscopic boundaries for being a SNR and as such would qualify for a (super)bubble. However, as for J0549–6618, the stellar environment shows no nearby massive stars which is a strong argument against a (super)bubble classification.

This paper has been typeset from a TEX/LATEX file prepared by the author.

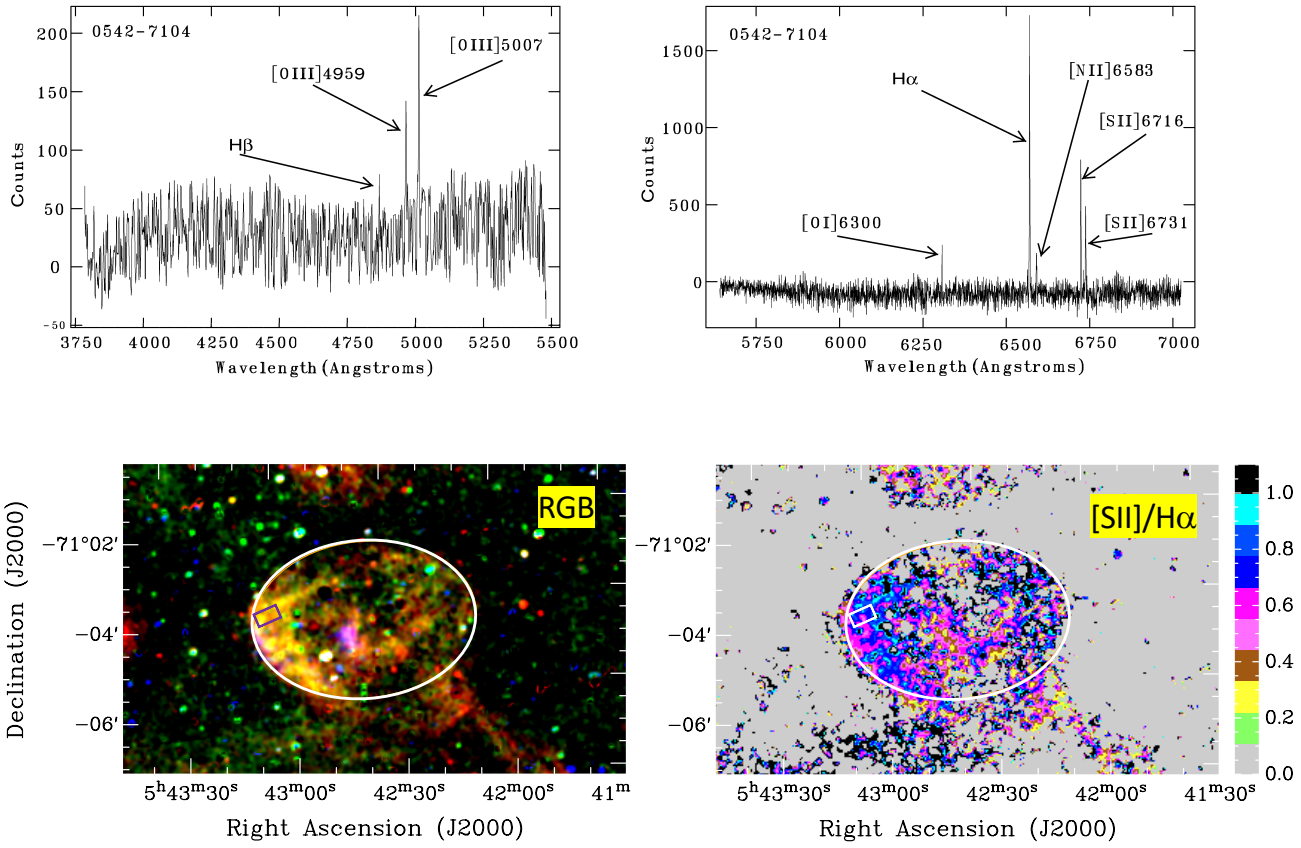

Figure A18. MCSNR J0542–7104: (Top) showing the spectra from both arms (left; blue, right; red) of the spectrograph; (Bottom) colour images produced from MCELS data, where RGB corresponds to Hα, [S II] and [O III] while the ratio map is between [S II] and Hα. The rectangular box (magenta/white) represents an approximate position of the WiFeS slicer. The white ellipse indicates the location of the optical shell.

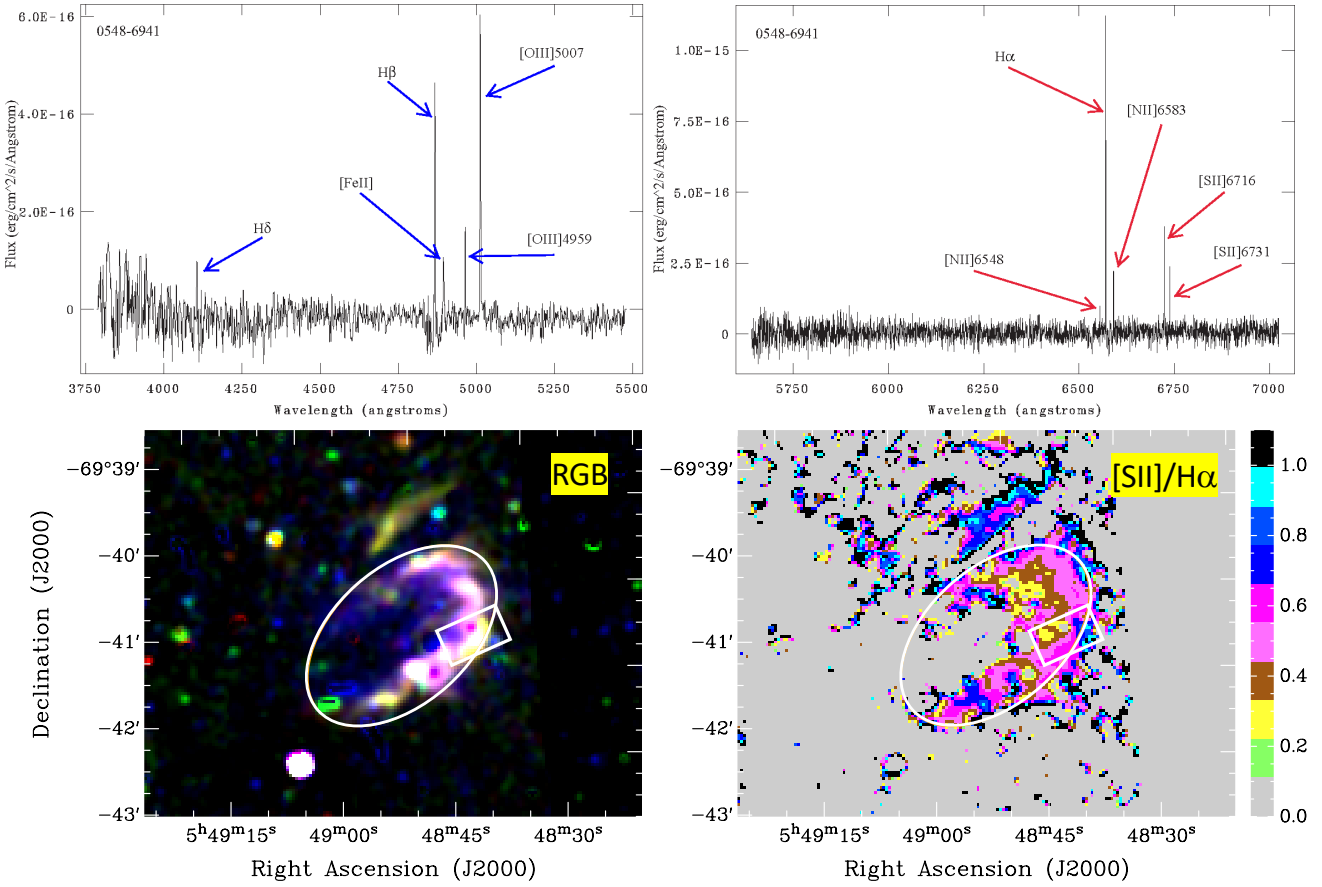

Figure A19. J0548–6941: (Top) showing the spectra from both arms (left; blue, right; red) of the spectrograph; (Bottom) colour images produced from MCELS data, where RGB corresponds to Hα, [S II] and [O III] while the ratio map is between [S II] and Hα. The rectangular box (white) represents an approximate position of the WiFeS slicer. The white ellipse indicates the location of the optical shell.

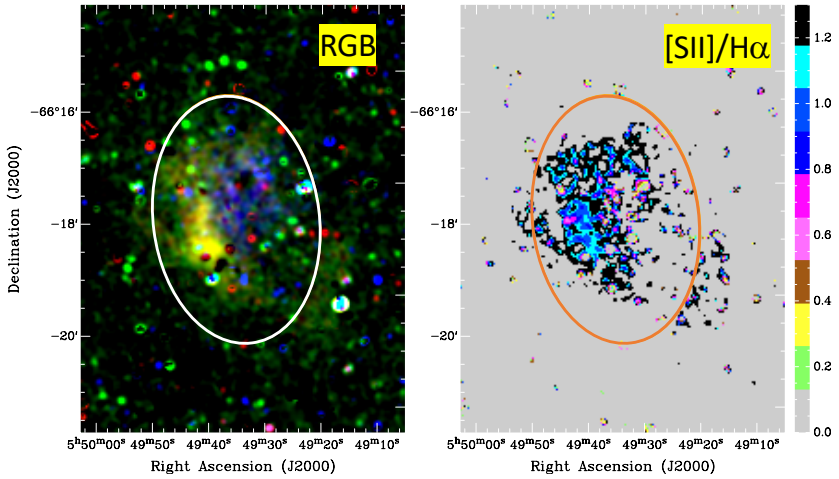

Figure A20. J0549–6618: colour images produced from MCELS data, where RGB corresponds to Hα, [S II] and [O III] while the ratio map is between [S II] and Hα. The white/orange ellipse indicates the location of the optical shell.

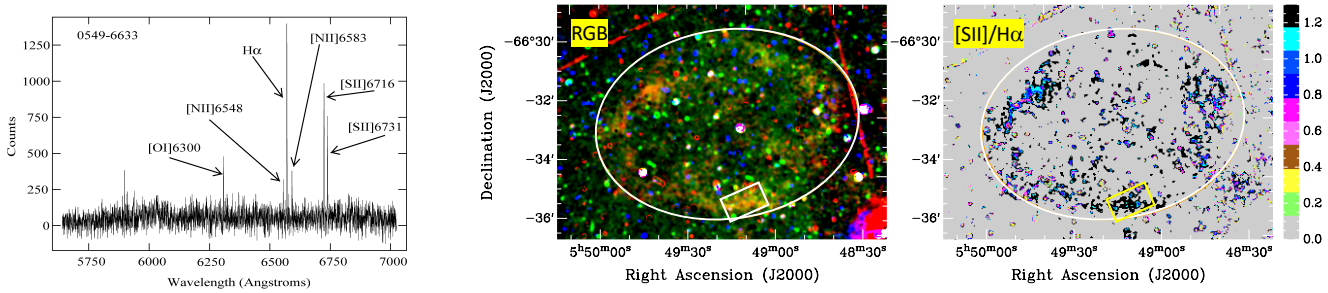

Figure A21. 0549–6633: (Left) showing the spectra from one arm (red) of the spectrograph; (Middle and right) colour images produced from MCELS data, where RGB corresponds to Hα, [S II] and [O III] while the ratio map is between [S II] and Hα. The rectangular box (white/yellow) represents an approximate position of the WiFeS slicer. The white ellipse indicates the location of the optical shell.